Studies of Si/SiO_2 Heterostructures Using Second Harmonic Generation

By

Xiong Lu

Dissertation

Submitted to the Faculty of the

Graduate School of Vanderbilt University

in partial fulfillment of the requirements

for the degree of

DOCTOR OF PHILOSOPHY

in

Physics

August, 2008

Nashville, Tennessee

Approved:

Professor Norman H. Tolk

Professor Royal G. Albridge

Professor Thomas W. Kephart

Professor Sait A. Umar

Professor Jimmy L. Davidson

Professor Ronald Schrimpf

To my parents

and my sisters,

for their never-ending love, support and sacrifice.

ACKNOWLEDGEMENTS

I would like to take this chance to express my great gratitude and appreciation for all the precious help I received during my Ph.D. study at Vanderbilt University.

First of all, I would like to thank my advisor, Professor Norman Tolk for the opportunity to be a part of his research group and all the valuable advice on my studies and research work. I would also like to thank my committee members, Professor Royal Albridge, Professor Jimmy Davidson, Professor Sait Umar， Professor Ronald Schrimpf and Professor Thomas Kephart for their helpful and timely suggestions, comments and discussions.

Second of all, I would like to thank the past and present members of the Center for Molecular and Atomic Studies at Surfaces (CMASS) research group, especially Dr. Robert Pasternak, Dr. Keith Miller, Dr. Yelena White, Dr. Ying Xu, Jingbo Qi, Travis Wade, Justin Gregory, Heungman Park, for their cooperation and discussions on the experiments.

Also, I would like to thank the Vanderbilt staff, especially the Physics office staff, Donald Pickert, Jane Fall, Barbara Amann, Sandy Childress, Eric Dye, the Physics science shop staff, John Fellenstein, the FEL staff, John Kozub. Without their friendly help, my studies and work at Vanderbilt wouldn't be as enjoyable as it is.

Last but not least, I would like to thank my parents for their unending love, support and sacrifice. It is their encouragement and support that hold me through this Ph.D. study and work during these years. I also would like to thank my sisters, especially my twin sister, Ying. They helped me to realize that life is precious and full of fun and sometimes I just need to take time to relax and enjoy. Without them I wouldn't be able to see this day of the completion of my Ph.D. thesis.

TABLE OF CONTENTS

Page

DEDICATION……... II

ACKNOWLEDGEMENTS ……III

LIST OF TABLES……VII

LIST OF FIGURES……...XI

Chapter

I. INTRODUCTION……**1**

1.1. Thesis introduction……..1
1.2. Review of Si and Si/SiO_2 ……5
1.3. Theory of second harmonic generation (SHG)……..12
1.4. Properties of second-order nonlinear susceptibility $\chi_{ijk}^{(2)}$ ……...18
1.5. Summary…….22

II. SECOND HARMONIC GENERATION AT SI/SIO2 INTERFACES, BACKGROUND…....…….23

2.1. Introduction……23
2.2. Angstrom-scale micro-roughness at the Si/SiO_2 interface probed by SHG..…….25
2.3. Stress relaxation at Si/SiO_2 system monitored by SHG……26
2.4. Summary……29

III. ELECTRIC-FIELD INDUCED SECOND HARMONIC GENERATION (EFISH), BACKGROUND……..….31

3.1. Introduction……31
3.2. Photo-excitation at the Si/SiO_2 interfaces……..35
3.3. Photo-induced EFISH monitoring $Si/(ZrO)_x(SiO_2)_{1-x}$ structure……..38
3.4. Photo-induced EFISH as a technique for measuring band-offset……..40
3.5. Charge trapping in irradiated SOI wafers measured by SHG……42
3.6. Summary……45

IV. EXPERIMENT CONFIGURATION……46

4.1. Introduction……...46
4.2. Ti:sapphire laser……46
4.3. The One-beam SHG technique…….……49
4.4. The Two-color SHG technique……..52
4.5. Summary……54

V. SECOND HARMONIC GENERATION FROM SILICON-ON-INSULATOR (SOI) STRUCTURES……..55

5.1. Introduction……55
5.2. SOI structures characterized and monitored by SHG……57
5.3. Fabrication of SOI wafers……..58
5.4. Sample preparation……60
5.5. Experimental setup……62
5.6. Experimental results and discussions……63
5.7. SHG as a potential process control tool……..69
5.8. Conclusions……72

VI. MULTI-INTERFACE SI/SIO2/MGO STRUCTURES STUDIED BY SECOND HARMONIC GENERATION……73

6.1. Introduction……..73
6.2. Energy band diagram……...75
6.3. Experimental setup and procedure……...77
6.4. Experimental results and discussions……...79
6.5. Conclusions……..84

VII. TEMPERATURE DEPENDENT SECOND- AND THIRD-ORDER SUSCEPTIBILITIES AT THE SI/SIO2 INTERFACE……..……85

7.1. Introduction……..85
7.2. Experimental configurations and procedure……86
7.3. Experimental results and discussions……...90
7.3.1. Temperature dependence of second-order susceptibility……...90
7.3.2. Temperature independent photo-induced electric field……..93
7.3.3. Temperature dependence of third-order susceptibility……...97
7.3.4. Temperature dependence of the trapping rate $\frac{1}{\tau^{e}_{trapping}}$ ……..99
7.4. Conclusions……102

VIII. SUMMARY……..104

LIST OF FIGURES

Figure **Page**

1.1. (a) The diamond-cubic crystal of silicon, with atoms on the cube corners and faces in red, and those inside in blue. (b) The illustration shows the arrangement of the silicon atoms in a unit cell, with the numbers indicating the height of the atom above the base of the cube as a fraction of the cell dimension…….6

1.2. Band diagram of Si/SiO_2 system……..11

1.3. (a) Geometry of second harmonic generation. (b) Energy-level diagram illustrating second harmonic generation……14

1.4. Correlation between the applied field *E(t)*, the potential energy *U(x)* and the polarization *P(t)* for centrosymmetric and noncentrosymmetric materials ……...……...16

1.5. Schematic of *p*-polarized light interacting with a Si surface resulting in the generation of second harmonic generation……20

2.1. Surface SH intensity vs. φ in re-oxidized Si(100), *p-p* configuration (open-circles, top panel), and *p-s* configurations (filled circles, middle panel). The solid lines are the corresponding fits to the data. The corresponding AFM scans in the bottom panel show measured rms values of 0.8, 1.5, and 2.7 A, respectively[27] …….....26

2.2. Azimuthal rotation dependence of the SH intensity from $Si(111)/SiO_2$ interfaces which were (a) unannealed, (b) hydrogen annealed for 120 minutes, (c) nitrogen annealed for 120 minutes. Solid curves are the fits using equation (2.8)[39]…….. ..28

2.3. Annealing time dependence of (a) χ_{zxx} and (b) χ_{xxx} for hydrogen-annealed and nitrogen-annealed samples[39]……..29

3.1. SHG from an oxidized *n*-Si(001) sample illuminated laser pulses at an angle of incidence of 80° (a) at average irradiance of 1.3 $kWcm^{-2}$ (beam B1), with a second 3.6 $kWcm^{-2}$ (beam B2) at normal incidence; and (b) at average irradiance of 0.5 $kWcm^{-2}$, with a normal incidence ultraviolet beam at the photon energies indicated……35

3.2. SHG signal observed from oxidized *n*-Si(100) after the ambient oxygen pressure is increased from 10^{-2} to 760 Torr in 2 s. The inset shows the

pressure dependence of the steady-state SHG intensity for increasing (crosses) and decreasing (circles) pressure. The data sets are offset for clarity[47]…….37

3.3. Oxide thickness dependence of the steady-state SHG from p-Si(100) for constant irradiance of 0.25 kW cm^{-2} at tan angle of incidence of 45°. The horizontal line indicates the quiescent level observed for all samples. The inset shows a schematic diagram of a possible electron excitation or transfer process[47]…….....37

3.4. EFISH signal from the interface of $Si/(ZrO)_x(SiO_2)_{1-x}$. The photon energy is 1.56 eV, the laser power varies between 300 and 560 mW. The inset shows the dependence of the SHG signal at t = 0 *vs* laser power on a log-log scale[9]……..39

3.5. The order of electron injection process from Si into SiO_2 *vs*. the photon energy of the pump beam, determined from the intensity dependence of injection rates[47].……...……41

3.6. (Left) Examples of SHG signals from region II of samples with BOX thickness of T_{Si} = 145 nm and 230 nm. Inset shows Region II which contains two interfaces (Si film/BOX and BOX/substrate). (Right) Schematic energy band diagrams of Si/BOX/substrate regions[8]….42

3.7. (Left) Examples of SHG signals with an external bias applied to the substrate prior to the laser beam illumination; (a) 40 V on the substrate and (b) – 40 V on the substrate. (Right) Schematic energy band diagrams of substrate/BOX regions. In (b) and (c), the internal fields are compensated and illustrated as light gray. The dark grey indicates the electric field due to charge separation[8]……...43

3.8. Example of SHG signals versus substrate bias before and after the total dose of 5 Mrad. T_{Si} = 72 nm and T_{BOX} = 230 nm[8]……...44

4.1. The schematic diagram of a typical self mode-locked Ti:sapphire laser.[60]……..48

4.2. The schematic diagram of a single-beam SHG setup……..49

4.3. A typical TD-EFISH measurement from a Si(100)/SiO_2 sample. The top layer is thermally grown 1.7 nm SiO_2……50

4.4. Schematic diagram of the two-color SHG technique……...52

4.5. Typical TP-EFISH response from the Si/SiO_2 system with two-color technique. Oxide layer thickness is 1.7 nm..……...53

5.1. (Left) The Schematic front view of wafer showing locations of contamination introduction. Note that contamination was introduced on the back of the wafers in concentrations shown as in solution. (Right) Descriptions of the specifications of the wafer……61

5.2. Microwave photoconductivity decay (μPCD) images of three SOI wafers with Ni, Cu, Fe contaminations at different locations on the back……..61

5.3. Microwave photoconductivity decay (μPCD) images of three Si/SiO_2 wafers with Ni, Cu, Fe contaminations at different locations on the back……..62

5.4. Conceptual schematic of the SHG configuration from a SOI wafer after removing the top native oxide layer[74]…….……63

5.5. SIMS data for intentionally contaminated wafers following the diffusion anneal[74]…….……...64

5.6. TD-SHG signals from the samples with (a) Ni contaminations, (b) Cu contaminations and (c) Fe contaminations. Also SHG signals from the reference samples are also shown for a comparison. Noted these set of samples are after HF etching treated, which means the top native oxide layer is etched off.……66

5.7. Correlation of microwave photoconductivity decay (μPCD) lifetime and peak SHG signal for intentionally Ni contaminated wafer after diffusion anneal. The inset shows the μPCD map and the arrows indicate the locations where SHG measurements were performed[74]……..67

5.8. Correlation of microwave photoconductivity decay (μPCD) lifetime and peak SHG signal for intentionally Cu contaminated wafer after diffusion anneal. The inset shows the μPCD map and the arrows indicate the locations where SHG measurements were performed[74]…….….67

5.9. The TD-SHG measurements from Ni contaminated samples and control sample (a) with native oxide and (b) without native oxide…….….68

5.10. The TD-SHG signals from SIMOX SOI wafers fabricated using two different recipes. Insets show the AFM images for the top Si/BOX interface.[71]……69

5.11. The TD-SHG signals from bonded SOI wafers fabricated using different thermal processing. Insets show the pseudo-MOSFET transfer characteristic measurements.[71]……...70

5.12. The TD-SHG experimental data normalized and combined to show schematically the potential and practical use of SHG for process control metrology[74].……71

6.1. The schematic band diagram of Si/SiO_2 structure……75

6.2. The schematic band diagram of $Si/SiO_2/MgO$ structure[76]……...76

6.3. A conceptual schematic of SHG from a $Si/SiO_2/MgO$ structure…….78

6.4. TD-SHG signals from the $Si/SiO_2/MgO$ structures at (a) high laser power of 620 mW and (b) low laser power of 240 mW. Smaller figures on the right are TP-SHG signals from Si/SiO_2 structure with a thickness of 2.4 nm[76]……...79

6.5. Schematic band diagrams of (a) $Si/SiO_2/MgO$ and (b) Si/SiO_2[76]…81

6.6. TD-SHG signal at laser power of 300 mW from (a) $Si/SiO_2/MgO$ structure and (b) Si/SiO_2 structure……...83

7.1. Time dependent EFISH data from $Si(100)/SiO_2$ with a 4.2 nm thermally grown oxide layer.……...……88

7.2. TD-EFISH measurements from a $Si(100)/SiO_2$ (4.2 nm) interface as a function of temperature[83].……91

7.3. Temperature dependence of the second-order nonlinear susceptibility [83]…….....93

7.4. Temperature dependence of EFISH saturation intensities[83]…….96

7.5. Temperature dependence of the third-order nonlinear susceptibility [83]……...98

7.6. Temperature dependence of the trapping rate $\frac{1}{\tau^{e}_{trapping}}$ for Si/SiO_2 [83]…….100

LIST OF TABLES

Table **Page**

1.1. Properties of Si ……..……...……. 8

1.2. Properties of SiO_2 ……..……...…10

6.1. Properties of MgO ..……...…..74

CHAPTER Ⅰ

INTRODUCTION

1.1. Thesis introduction

In this thesis, we report on second harmonic generation (SHG) experiments on Si/SiO_2, silicon-on-insulator (SOI) and $Si/SiO_2/MgO$ heterostructure systems. These experiments have led to an enhanced understanding of the optical properties of these systems and of the charge carrier dynamics associated with the photo-induced electric field.

Second harmonic generation is the simplest nonlinear optical process in which the atomic response to a high intensity laser depends quadratically on the strength of the applied optical field. This phenomenon was first demonstrated by Franken *et al.* in 1961[1]. This group used pulses from a ruby laser, first built by Maiman in 1960[2]. On passage of the ruby laser pulse of wavelength 694.3 nm through a quartz crystal, some ultraviolet photons at twice the frequency were generated. After passage through a monochromator, they produced some faint spots on a photographic plate. Unfortunately, the editorial office of *Physical Review Letters* removed these spots as undesirable smudges and the paper was rejected. However, this work is often taken to be the beginning of the field of nonlinear optics.

Franken also had sent a preprint of his SHG paper to Nicholas Bloembergen's research group at Harvard. This group immediately initiated a theoretical investigation into the newly observed phenomenon in the summer of 1961. This effort resulted in a series of theoretical papers, of which one dealt with the behavior of light waves at the boundary of a nonlinear medium[3]. After this group acquired its first ruby laser, they concentrated on SHG in optically absorbing materials. They measured the nonlinear optical properties of GaAs in reflection and verified the predicted laws of nonlinear reflection[4, 5]. In the process, they measured both the real and imaginary part of the complex second-order nonlinear susceptibility[6]. The pioneering experiments in the sixties were all carried out with ruby lasers. The potential of nonlinear optics as a surface-specific tool was not fully exploited until the decade of the eighties. With the invention of the tunable pulsed dye laser systems, pulsed Ti:sapphire lasers and tunable optical parametric oscillators in the eighties, more quantitative investigations became possible. Pump-probe techniques with picosecond and femtosecond laser systems also enabled investigations of the dynamics of surface processes, including the absorption, desorption, and surface diffusion of atoms and molecules.

Many sophisticated SHG experiments using Ti:sapphire lasers and optical parametric generators were carried out in the late eighties and nineties. Because the second-order nonlinear susceptibility vanishes in a material with a center of inversion of symmetry such as silicon, it makes second harmonic generation potentially into a very useful surface/interface sensitive probing tool. More recently, electric field induced second harmonic generation (EFISH) has been used to study charge carrier dynamics in

semiconductor/insulator systems[7-9]. This approach provides information on carrier injection, transport, trapping, de-trapping and recombination processes in the thin layers of semiconductor/insulator devices, which is difficult or impossible to obtain using conventional electrical measurements.

The thesis treats three topics each involving second harmonic generation. Firstly, we report SHG measurements on SOI wafers which have been intentionally contaminated. Our experiments show that the SHG response is radically different depending on roughness, defects, and/or contamination at the interface. Compared to conventional silicon processing, SOI technology improves power consumption of the devices because of the lower parasitic capacitance, which makes SOI technology an increasingly important technology in the modern semiconductor industry. The conventional way of characterizing an SOI wafer involves physical contact with the wafer thus significantly increasing the probability of damage to the wafer. Our experiments on SOI wafers show SHG is sensitive to the buried interface roughness, contamination and defects. The contactless and nondestructive SHG technique shows promise of providing an alternative to conventional electrical measurement techniques for characterizing the wafers.

Secondly, we report our work on $Si/SiO_2/MgO$ structures. Our measurements show that time dependent electric induced SHG responses from Si/SiO_2 and $Si/SiO_2/MgO$ are drastically different. We suggest a potential well is created at the interface of SiO_2 and MgO during the deposition of MgO layer. This potential well provides higher density of states and these electron trap states have a lower energy barrier than those at the SiO_2

surface. Moreover, defects are possibly introduced in the SiO_2 near the interface of two oxides during the deposition. These defects facilitate the tunneling of the electrons through the oxide which then recombine with holes. Our measured power dependence in the SHG experiment suggests that, 1) at high laser power, the electron injection and trapping process dominates the carrier dynamics at the interfaces, 2) at low laser power, hole injection dominates which allows us to observe different SHG responses arising from the hole injection process.

Thirdly, we employed a unique two-color SHG approach to our temperature dependence work on Si/SiO_2. The EFISH intensity can be expressed as a function of the interfacial photo-induced electric field, involving both second- and third-order nonlinear susceptibilities. Our temperature dependent EFISH data shows that the magnitude of the second-order nonlinear susceptibility increases as temperature increases. We also conclude that the photo-induced electric field, which is directly related to the number of filled electronic states on the SiO_2 surface, doesn't vary with temperature. From the experimental data, we deduce that the third-order nonlinear susceptibility also increases as temperature increases. Therefore, the temperature dependence of the EFISH saturation intensity is entirely due to the temperature dependence of second- and third-order nonlinear susceptibilities. We also determine that the temperature dependence of the rise time of the EFISH intensity is a combination effect of electron-phonon scattering, temperature dependence of Si absorption coefficient and SiO_2 refractive index.

The work reported in this thesis illustrates that second harmonic generation is a very efficient, sensitive, contactless, and nondestructive surface/interface technique.

1.2. Review of Si and Si/SiO_2

The work reported in this thesis is closely related to the material and optical properties of Si and SiO_2. The following is a brief review of the properties of Si and SiO_2.

Silicon was discovered by Jöns Jacob Berzelius, a Swedish chemist, in 1824 in the process of heating chips of potassium in a silica container and then carefully washing away the residual by-products[10]. As the eighth most common element in the universe by mass, silicon occasionally occurs as a pure free element in nature, but is more widely distributed in dusts, planetoids and planets as various form of silicon dioxide or silicate. Also, measured by mass, silicon makes up 25.7% of the Earth's crust and is the second most abundant element on Earth, with oxygen being the first (46.7% by mass).

Silicon is widely used in industry. The largest application of pure silicon is in aluminum-silicon alloys, often called 'light alloys', to produce cast parts, mainly for the automobile industry. Elemental silicon is also the principal component of most semiconductor devices, most importantly integrated circuits, transistors, solar cells or microchips. An essential aspect of silicon based devices is doping pure silicon with other elements to adjust its electrical response by controlling the number and charge of current carriers. In the form of silica and silicates, silicon forms useful glasses, cements, and ceramics.

Silicon is also a major component of silicones, which are compounds containing silicon-oxygen and silicon-carbon bonds that have the capability to act as bonding intermediates between glass and organic compounds, and to form polymers[11, 12].

Silicon is widely used in the semiconductor industry and the purity and quality of semiconductor grade silicon (SGS) are important factors. There are three basic steps to obtain pure silicon. First, produce metallurgical grade silicon (MGS) by heating silica with carbon in a furnace. Second, purify metallurgical grade silicon through a chemical reaction to a silicon-bearing gas trichlorosilane ($SiHCl_3$). Last, $SiHCl_3$ and hydrogen react in a CVD process to produce pure semiconductor-grade silicon.

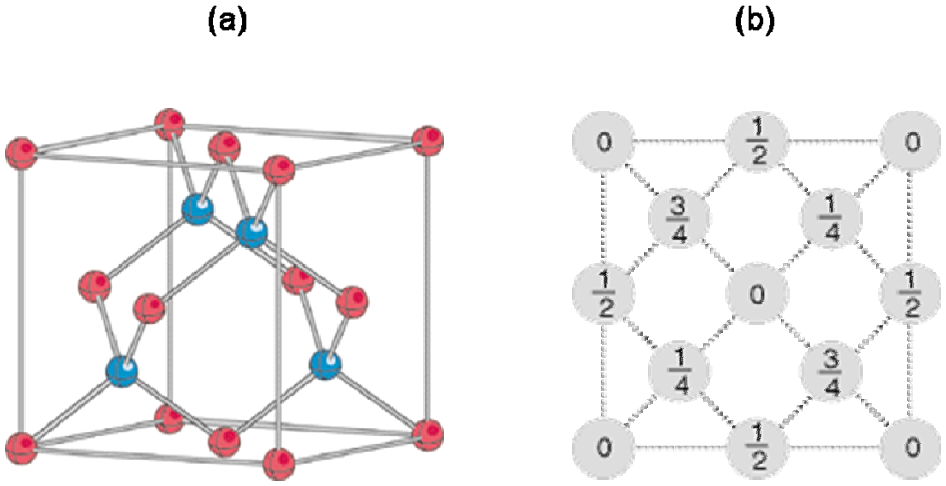

Figure 1.1 (a) The diamond-cubic crystal of silicon, with atoms on the cube corners and faces in red, and those inside in blue. (b) The illustration shows the arrangement of the silicon atoms in a unit cell, with the numbers indicating the height of the atom above the base of the cube as a fraction of the cell dimension.

Silicon crystallizes in the diamond cubic structure, as shown in figure 1.1 (a), which is responsible for the hardness of the diamond form of carbon. Notice that each atom has four neighbors at the corners of a tetrahedron. If, in some defect structure, a silicon atom has fewer than four neighbors, it is said to have dangling bonds. In figure 1.1 (b) the illustration shows the arrangement of the silicon atoms in a unit cell. The lines between silicon atoms indicate the nearest-neighbor bonds. The cube side of silicon is 5.43 $\mathring{A}$.

The diamond-cubic crystal structure gives silicon special material properties; Table 1.1 summarizes the basic parameters of silicon at room temperature (300K).

Table 1.1. Properties of Si[13-15]

Property	Value	Unit
Atoms/cm^3	5×10^{22}	
Atomic Weight	28.9	
Bulk Modulus	9.8×10^{11}	dyn/cm^2
Density	2.329	$g\ cm^{-3}$
Dielectric constant	11.7	
Energy Gap	1.12	eV
Electron Affinity	4.05	eV
Infrared Refractive Index	3.42	
Intrinsic Carrier Concentration	1×10^{10}	cm^{-3}
Intrinsic Resistivity	3.2×10^5	Ω cm
Lattice Constant	5.431	$\mathring{A}$
Melting Point	1412	°C
Mobility Electrons	< 1400	$cm^2\ V^{-1}\ s^{-1}$
Mobility Holes	≤450	$cm^2\ V^{-1}s^{-1}$
Optical Phonon Energy	0.063	eV
Thermal Conductivity	1.3	$W\ cm^{-1}\ (°C)^{-1}$
Thermal Diffusivity	0.8	cm^2/s
Thermal expansion, linear	2.6×10^{-6}	$(°C)^{-1}$

SiO_2, silicon dioxide, also known as silica is mechanically very stable. It is formed by strong, directional covalent bonds, and has a well-defined local structure, where four oxygen atoms are arrayed at the corners of a tetrahedron around a central silicon atom. It is a group IV metal oxide and has good abrasion resistance, electrical insulation and high thermal stability. SiO_2 not only can largely passivate silicon but also can isolate the devices from the ambient to minimize electrostatic effects.

The Si-O-Si has a high rotational flexibility. Thus SiO_2 often forms a glassy, continuous random network (CRN) structure[16]. This high flexibility helps the creation of saturated bonds at the interface when forming an interface with silicon. The remaining dangling bonds are normally saturated by hydrogen or OH. Table 1.2 summarizes the most important electronic and material properties of SiO_2.

Table 1.2. Properties of SiO_2 [13-15, 17]

Property	**Value**	**Unit**
Atomic Weight	60	
Crystal Structure	amorphous	
DC Resistivity at 25 C	10^{14} - 10^{16}	Ω cm
Density	2.2	g/cm^3
Dielectric Constant	3.9	
Dielectric Strength	10^7	V/cm
Energy Gap at 300K	9	eV
Infrared Absorption Band	9.3	μm
Melting Point	~ 1600	°C
Mobility Electrons	20	$cm^2\ V^{-1}\ s^{-1}$
Mobility Holes	~ 10^{-6}	$cm^2\ V^{-1}s^{-1}$
Refractive Index	1.46	
Thermal expansion	5 x 10^{-7}	$(°C)^{-1}$

To fully understand the charge carrier dynamics at semiconductor-insulator interfaces, we have to understand the band structure at the interface. Figure 1.2 shows the most widely acknowledged local band structure of Si/SiO_2 system[18]. As indicated in the figure, the barrier for electron injection is 3.2 eV, starting from the conduction band of silicon. Correspondingly, it is 4.6 eV for hole injection starting from the valence band of silicon. For electron external photoemission, an extra 1 eV is necessary. The additional energy is the difference between the vacuum level and the SiO_2 conduction band.

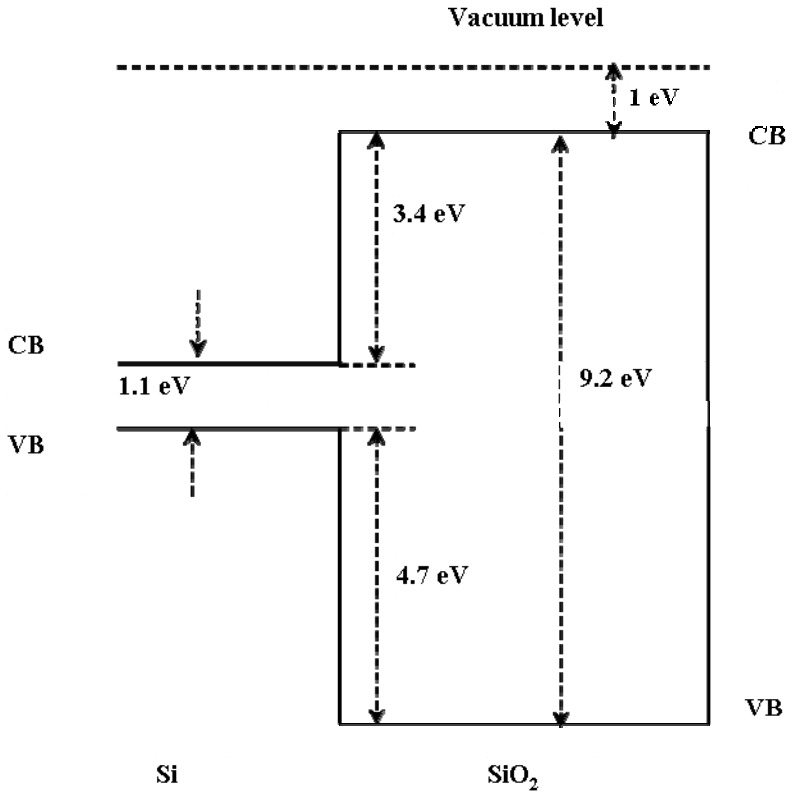

Figure 1.2. Band diagram of the Si/SiO_2 system.

It is worthwhile to notice that the barrier for hole injection from the Si valance band to SiO_2 valance band (4.6 eV) is higher than that of electron injection from the Si valance band to SiO_2 conduction band (4.3 eV). The lower barrier for electron injection makes it dominant in most of the studies. The higher energy barrier for hole injection may require a higher order photon excitation process than the electron injection process depending on the wavelength of the laser used. Therefore in many optical studies hole injection is very hard to observe. However, when laser intensity is relatively high, hole injection has been detected[19].

1.3. Theory of second harmonic generation (SHG)

Under normal conditions the response of a medium to light is linear, and as a consequence most optical phenomena can be described with a linear refractive index. With the invention of lasers in the early 1960's, the available optical power level was high enough to change the response of the medium from linear to nonlinear. It opened a new era of nonlinear optics and discoveries of various intriguing phenomena such as sum- and difference-frequency generation[20, 21].

Nonlinear optics studies the phenomena that occur as a consequence of the modification of the optical properties of a material system by the presence of light. Nonlinear optical phenomena are 'nonlinear' in the way that they occur when the material system responds to the applied optical field in a nonlinear manner. To better understand the optical

nonlinearity, we consider how a material system responds to an applied optical field in terms of polarization $\vec{P}(t)$ and field strength $\vec{E}(t)$.

In linear optics, the induced polarization $\vec{P}(t)$ depends linearly on the strength of the applied optical field $\vec{E}(t)$, which can be described as

$$\vec{P}(t) = \chi^{(1)}\vec{E}(t) \tag{1.1}$$

where $\chi^{(1)}$ is the linear susceptibility, a second rank tensor.

In nonlinear optics, we express the polarization $\vec{P}(t)$ as a Taylor expansion in a power series of the field strength $\vec{E}(t)$,

$$\vec{P}(t) = \chi^{(1)}\vec{E}(t) + \chi^{(2)}\vec{E}^2(t) + \chi^{(3)}\vec{E}^3(t) + \ldots = \vec{P}^{(1)}(t) + \vec{P}^{(2)}(t) + \vec{P}^{(3)}(t) + \ldots \tag{1.2}$$

where $\chi^{(2)}$ is the second-order nonlinear susceptibility and $\chi^{(3)}$ is the third-order nonlinear susceptibility and so on. We refer to $\vec{P}^{(2)}(t)$ as the second-order nonlinear polarization and $\vec{P}^{(3)}(t)$ as the third-order nonlinear polarization and so on.

The most common procedure for describing nonlinear optical phenomena is based on expressing the polarization $\vec{P}(t)$ in terms of the applied electric field strength $\vec{E}(t)$, as we did in equation (1.2).

SHG is the simplest nonlinear optical process and can be illustrated schematically in Figure 1.3 (a). According to this illustration, a laser beam of frequency ω impinges upon a crystal surface and a laser beam of frequency 2ω is generated. In quantum mechanical terms, the SHG process can also be visualized by considering the interaction of photons as shown in Figure 1.3 (b). It shows that two photons of the same frequency ω and energy $\hbar\omega$ are destroyed and a photon of frequency 2ω energy $2\hbar\omega$ is simultaneously created in a single quantum-mechanical process. The horizontal solid line represents the atomic ground state and dashed lines represent the virtual states.

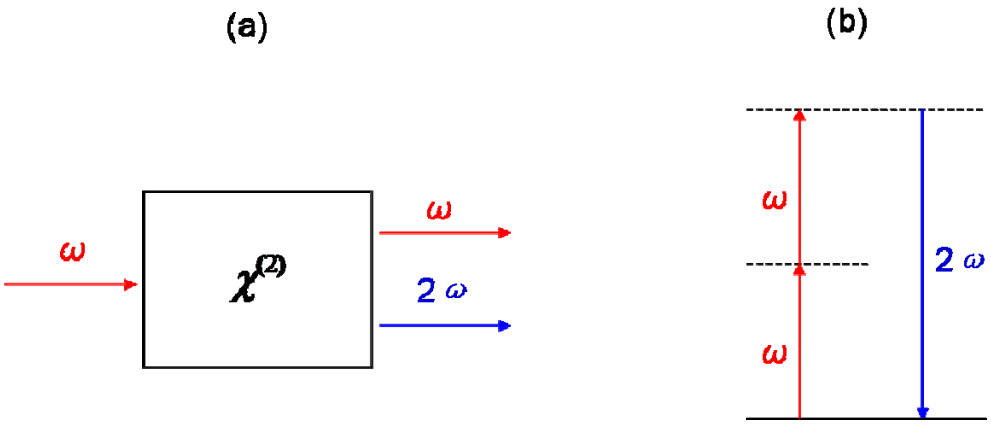

Figure 1.3 (a) Geometry of second harmonic generation. (b) Energy-level diagram illustrating second harmonic generation.

When the incident light interacts with the material, electrons oscillate within a potential well with a restoring force. The restoring force obeys Hooke's Law, that is the force is a function of the displacement of the electron from its equilibrium position. The potential energy curve is approximately harmonic. However, if the incoming field is sufficiently high, the interaction becomes nonlinear and the restoring force no longer increases linearly with the displacement. Thus Hooke's Law is violated. The potential energy curve deviates from a parabola. The manner in which the energy curve deviates from a perfect parabola depends on the molecular structure of the material itself. Molecular structures can be classified into two general categories: those with a center of symmetry (centrosymmetric) and those without (noncentrosymmetric). Figure 1.4 shows potential energies for both categories of matter. Second harmonic generation can be expressed in terms of the nonlinear polarization oscillating at the frequency of 2ω (ω is the frequency of the applied field)[22].

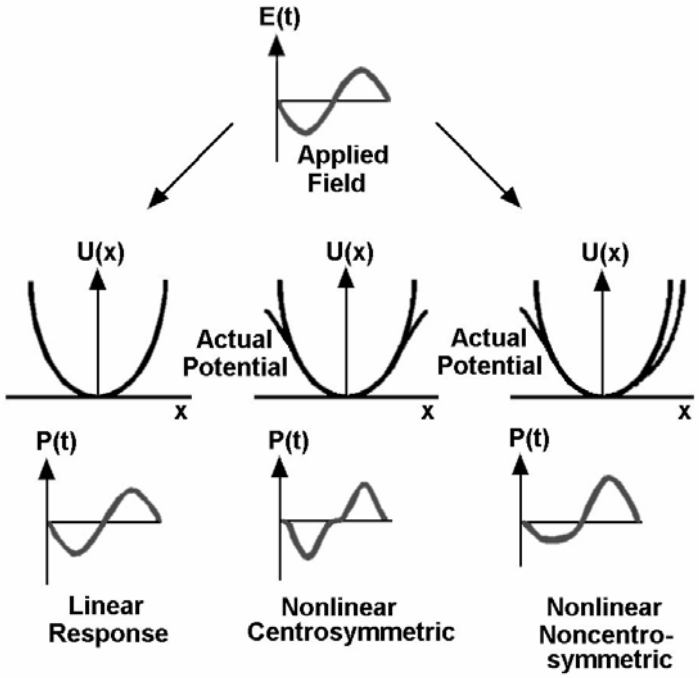

Figure 1.4. Correlation between the applied field *E(t)*, the potential energy *U(x)* and the polarization *P(t)* for centrosymmetric and noncentrosymmetric materials[22].

The electric filed strength of the incident laser beam can be described as

$$\vec{E}(t) = Ee^{-i\omega t} + c.c. \tag{1.3}$$

The second-order nonlinear polarization created in the crystal is given according to equation (1.2) as

$$\vec{P}^{(2)}(t) = \chi^{(2)}\vec{E}^2(t) = 2\chi^{(2)}EE^* + (\chi^{(2)}E^2e^{-2i\omega t} + c.c.) \tag{1.4}$$

The second-order polarization has two contributions, one from zero frequency (the first term) and one from the doubled frequency 2ω (the second term). The zero frequency contribution is responsible for the generation of a static electric field within the nonlinear crystal (a process known as optical rectification). The latter contribution generates the radiation at the second harmonic frequency. This is often used to convert the output from a laser to a different optical region. For example, in most of our experiment setups, the output from a Ti:saphhire laser is set to a wavelength of 800 nm. Second harmonic generation is then applied to convert the incident wavelength of 800 nm to 400 nm.

Let us consider the second term in the case of second harmonic generation. In SHG, the components of the second-order susceptibility tensor can be defined as proportionality constants relating the amplitude of the second-order polarization to the product of field amplitudes according to[20]

$$P_i^{(2)}(2\omega) = \sum_{jk} \chi_{ijk}^{(2)}(2\omega : \omega, \omega) E_j(\omega) E_k(\omega) . \tag{1.5}$$

Here the index i refers to the components of the second harmonic field, and j and k refer to the Cartesian components of the fundamental field.

1.4. Properties of second-order nonlinear susceptibility $\chi_{ijk}^{(2)}$

$\chi_{ijk}^{(2)}$ is a third-rank tensor which describes the second-order nonlinear optical susceptibility, an inherent property of the material. The index *i* refers to the component of the second harmonic field, and indices *j*, *k* refer to the Cartesian components of the fundamental field. For a lossless medium, all of the components $\chi_{ijk}^{(2)}$ are real. This result is obeyed for the classical anharmonic oscillator. It shows that the imaginary part of nonlinear susceptibility is determined by absorption coefficient of the material.

$\chi_{ijk}^{(2)}$ can be represented as a 3 x 9 matrix with 27 elements as

$$\chi_{ijk}^{(2)} = \begin{pmatrix} \chi_{xxx}^{(2)} & \chi_{xxy}^{(2)} & \chi_{xxz}^{(2)} & \chi_{xyx}^{(2)} & \chi_{xyy}^{(2)} & \chi_{xyz}^{(2)} & \chi_{xzx}^{(2)} & \chi_{xzy}^{(2)} & \chi_{xzz}^{(2)} \\ \chi_{yxx}^{(2)} & \chi_{yxy}^{(2)} & \chi_{yxz}^{(2)} & \chi_{yyx}^{(2)} & \chi_{yyy}^{(2)} & \chi_{yyz}^{(2)} & \chi_{yzx}^{(2)} & \chi_{yzy}^{(2)} & \chi_{yzz}^{(2)} \\ \chi_{zxx}^{(2)} & \chi_{zxy}^{(2)} & \chi_{zxz}^{(2)} & \chi_{zyx}^{(2)} & \chi_{zyy}^{(2)} & \chi_{zyz}^{(2)} & \chi_{zzx}^{(2)} & \chi_{zzy}^{(2)} & \chi_{zzz}^{(2)} \end{pmatrix}. \quad (1.6)$$

The individual elements of $\chi_{ijk}^{(2)}$ can be determined by different combinations of the directions of polarization and angles of the incident beam(s) and of the second harmonic beam. There are a number of restrictions resulting from symmetries that relate the various components, and hence fewer numbers of elements are usually needed in order to describe the nonlinear coupling.

First of all, the intrinsic permutation symmetry of $\chi_{ijk}^{(2)}$ has $\chi_{ijk}^{(2)} = \chi_{ikj}^{(2)}$, which makes $\chi_{ijk}^{(2)}$ symmetric in its last two indices. This is valid because the response of the medium cannot

depend on the mathematical ordering of the fields. Also, for second harmonic generation, the interfering ω_m and ω_n are equal. The form of $\chi_{ijk}^{(2)}$ now can be represented by a matrix with 16 independent elements as in (1.7).

$$\chi_{ijk}^{(2)} = \begin{pmatrix} \chi_{xxx}^{(2)} & \chi_{xxy}^{(2)} & \chi_{xxz}^{(2)} & \chi_{xxy}^{(2)} & \chi_{xyy}^{(2)} & \chi_{xyz}^{(2)} & \chi_{xxz}^{(2)} & \chi_{xyz}^{(2)} & \chi_{xzz}^{(2)} \\ \chi_{yxx}^{(2)} & \chi_{yxy}^{(2)} & \chi_{yxz}^{(2)} & \chi_{yxy}^{(2)} & \chi_{yyy}^{(2)} & \chi_{yyz}^{(2)} & \chi_{yxz}^{(2)} & \chi_{yyz}^{(2)} & \chi_{yzz}^{(2)} \\ \chi_{zxx}^{(2)} & \chi_{zxy}^{(2)} & \chi_{zxz}^{(2)} & \chi_{zxy}^{(2)} & \chi_{zyy}^{(2)} & \chi_{zyz}^{(2)} & \chi_{zxz}^{(2)} & \chi_{zyz}^{(2)} & \chi_{zzz}^{(2)} \end{pmatrix}. \tag{1.7}$$

Now, we can describe the nonlinear polarization leading to second harmonic generation in terms of $\chi_{ijk}^{(2)}$ by the matrix equation

$$\begin{pmatrix} P_x^{(2)} \\ P_y^{(2)} \\ P_z^{(2)} \end{pmatrix} = \begin{pmatrix} \chi_{xxx}^{(2)} & \chi_{xxy}^{(2)} & \chi_{xxz}^{(2)} & \chi_{xxy}^{(2)} & \chi_{xyy}^{(2)} & \chi_{xyz}^{(2)} & \chi_{xxz}^{(2)} & \chi_{xyz}^{(2)} & \chi_{xzz}^{(2)} \\ \chi_{yxx}^{(2)} & \chi_{yxy}^{(2)} & \chi_{yxz}^{(2)} & \chi_{yxy}^{(2)} & \chi_{yyy}^{(2)} & \chi_{yyz}^{(2)} & \chi_{yxz}^{(2)} & \chi_{yyz}^{(2)} & \chi_{yzz}^{(2)} \\ \chi_{zxx}^{(2)} & \chi_{zxy}^{(2)} & \chi_{zxz}^{(2)} & \chi_{zxy}^{(2)} & \chi_{zyy}^{(2)} & \chi_{zyz}^{(2)} & \chi_{zxz}^{(2)} & \chi_{zyz}^{(2)} & \chi_{zzz}^{(2)} \end{pmatrix} \begin{pmatrix} E_x E_x \\ E_x E_y \\ E_x E_z \\ E_x E_y \\ E_y E_y \\ E_y E_z \\ E_x E_z \\ E_y E_z \\ E_z E_z \end{pmatrix}. \tag{1.8}$$

If we combine the equivalent elements, matrix (1.8) can be rewritten in a contracted form

$$\begin{pmatrix} P_x^{(2)} \\ P_y^{(2)} \\ P_z^{(2)} \end{pmatrix} = \begin{pmatrix} \chi_{xxx}^{(2)} & \chi_{xyy}^{(2)} & \chi_{xzz}^{(2)} & \chi_{xxy}^{(2)} & \chi_{xxz}^{(2)} & \chi_{xyz}^{(2)} \\ \chi_{yxx}^{(2)} & \chi_{yyy}^{(2)} & \chi_{yzz}^{(2)} & \chi_{yxy}^{(2)} & \chi_{yxz}^{(2)} & \chi_{yyz}^{(2)} \\ \chi_{zxx}^{(2)} & \chi_{zyy}^{(2)} & \chi_{zzz}^{(2)} & \chi_{zxy}^{(2)} & \chi_{zxz}^{(2)} & \chi_{zyz}^{(2)} \end{pmatrix} \begin{pmatrix} E_x E_x \\ E_y E_y \\ E_z E_z \\ 2E_x E_y \\ 2E_x E_z \\ 2E_y E_z \end{pmatrix}. \tag{1.9}$$

Let us now consider the case of an incoming *p*-polarized light interacting with Si surface. The incident light is in the y-z plane as illustrated in figure 1.5. The reflection of the second harmonic generation beam is also in the y-z plane.

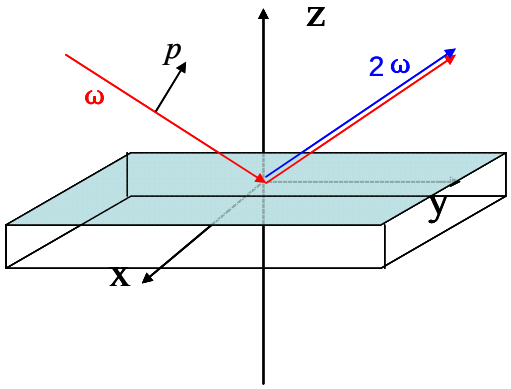

Figure 1.5. Schematic of *p*-polarized light interacting with a Si surface resulting in the generation of second harmonic radiation.

Since Si is centrosymmetric, we can apply the mirror-transformation to determine the nonzero elements of the $\chi_{ijk}^{(2)}$ matrix. After applying mirror-transformation to y-z and x-z planes, we find that there are only five nonzero elements, and they are,

$\chi^{(2)}_{yzy} = \chi^{(2)}_{xzx}, \chi^{(2)}_{zxx} = \chi^{(2)}_{zyy}, \chi^{(2)}_{zzz}$. Now, the nonlinear polarization leading to the second harmonic generation in (1.9) can be rewritten as

$$\begin{pmatrix} P_x^{(2)} \\ P_y^{(2)} \\ P_z^{(2)} \end{pmatrix} = \begin{pmatrix} 0 & 0 & 0 & 0 & \chi^{(2)}_{xxz} & 0 \\ 0 & 0 & 0 & 0 & 0 & \chi^{(2)}_{yyz} \\ \chi^{(2)}_{zxx} & \chi^{(2)}_{zxx} & \chi^{(2)}_{zzz} & 0 & 0 & 0 \end{pmatrix} \begin{pmatrix} E_x E_x \\ E_y E_y \\ E_z E_z \\ 2E_x E_y \\ 2E_x E_z \\ 2E_y E_z \end{pmatrix} . \tag{1.10}$$

If the incoming light is *p*-polarized, x component of the optical field is zero. In this condition, the nonlinear polarization becomes

$$\begin{pmatrix} P_x^{(2)} \\ P_y^{(2)} \\ P_z^{(2)} \end{pmatrix} = \begin{pmatrix} 0 & 0 & 0 & 0 & \chi^{(2)}_{xxz} & 0 \\ 0 & 0 & 0 & 0 & 0 & \chi^{(2)}_{yyz} \\ \chi^{(2)}_{zxx} & \chi^{(2)}_{zxx} & \chi^{(2)}_{zzz} & 0 & 0 & 0 \end{pmatrix} \begin{pmatrix} 0 \\ E_y E_y \\ E_z E_z \\ 0 \\ 0 \\ 2E_y E_z \end{pmatrix} = \begin{pmatrix} 0 \\ 2\chi^{(2)}_{yyz} E_y E_z \\ \chi^{(2)}_{zxx} E_y^2 + \chi^{(2)}_{zzz} E_z^2 \end{pmatrix}. \tag{1.11}$$

From (1.11), we can see that with an incoming *p*-polarized light, the generated second harmonic generation beam is also *p*-polarized with y and z components.

Here we only discuss the case for Si. Any additional symmetry properties of a nonlinear optical medium can impose additional restrictions on the form of the nonlinear susceptibility tensor. By explicit consideration of the symmetries of each of the crystal

classes, the allowed form of the susceptibility tensor for crystals of that class can be determined. The results of such calculation can be found in many text books, for example, *The Nonlinear Optical Susceptibility* by Boyd[21].

1.5. Summary

In this introductory chapter, we have discussed the material properties of Si and SiO_2 and introduced important elements of the theory of SHG. In chapter II, we will present a general treatment of SHG at the Si/SiO_2 interface, and also review some of the experiments from various groups using SHG to characterize the buried interface. In chapter Ⅲ, we will introduce electric field induced second harmonic generation (EFISH) and review relevant research done by others employing EFISH.

In chapter Ⅳ, we will take a historical view of the Ti:sapphire laser which is used in most of our experiments. We will describe the basic experimental techniques and configurations used in our work. In chapter Ⅴ through Ⅶ, we will present our work on SOI structures, $Si/SiO_2/MgO$ structures and temperature dependence of SHG on Si/SiO_2 structures, respectively. Chapter Ⅷ will summarize the discussions and conclusions of our work.

CHAPTER Ⅱ

SECOND HARMONIC GENERATION AT SI/SIO2 INTERFACES, BACKGROUND

2.1. Introduction

Si is a centrosymmetric crystal and SiO_2 as used in our research is an amorphous material without a regular crystalline order. Thus, second harmonic light is not generated in the bulk of Si or SiO_2. However, at Si/SiO_2 interface, the symmetry is broken and second harmonic generation is allowed. Also, previous scanning tunneling microscopy (STM) experiments by Heinz *et al.* has showed that the second harmonic generation signal mostly comes from the 2 to 3 topmost atomic layers[23]. This makes second harmonic generation very surface/interface sensitive in Si/SiO_2 structures. Much effort has been expended to use SHG to investigate buried interfaces. In this chapter, we will review significant work from various groups employing SHG to study Si/SiO_2 interfaces.

To demonstrate that second harmonic generation vanishes inside a centrosymmetric material, we assume that a nonlinear polarization is generated in such a crystal by using a single applied field. The components of second-order polarization will be given by equation (1.5) and the applied field is given by

$$\vec{E}(t) = \xi \cos \omega t \,. \tag{2.1}$$

Under the assumption that the medium possesses inversion symmetry, if we change the sign of the electric field, the induced polarization will also change the sign. Therefore according to equation (1.5), now we have

$$-P_i^{(2)} = \sum_{jk} \chi_{ijk}^{(2)}(-E_j)(-E_k) = \sum_{jk} \chi_{ijk}^{(2)} E_j E_k \,. \tag{2.2}$$

Comparison of equation (1.5) and (2.2) shows

$$P_i^{(2)} = -P_i^{(2)} \,. \tag{2.3}$$

which occurs only if $\vec{P}(t)$ vanishes. This is true only when

$$\chi_{ijk}^{(2)} = 0 \,. \tag{2.4}$$

Thus, we can conclude that the second-order nonlinear susceptibility of centrosymmetric crystals is zero.

The intensity of second harmonic generation signal can be described in terms of the second-order nonlinear polarization as

$$I^{(2\omega)} \propto | P^{(2)}(2\omega) |^2 \tag{2.5}$$

After substituting equation (1.5), we get

$$I^{(2\omega)} = |\chi_{eff}^{(2)}|^2 (I^{(\omega)})^2 \quad (2.6)$$

where $\chi_{eff}^{(2)}$ is the second-order nonlinear susceptibility describing the Si/SiO_2 interface and higher order sources such as bulk quadrupole. $I^{(\omega)} = E(\omega)E(\omega)$ is the fundamental beam intensity. From the equation, we can see that the intensity of the second harmonic generation signal depends quadratically on the intensity of the incident fundamental laser.

2.2. Angstrom-scale micro-roughness at the Si/SiO_2 interface probed by SHG

Normally, the surface oxide has to be removed to measure the angstrom-scale interface roughness. Yet, optical second harmonic generation has proven to be a sensitive noninvasive technique, which can probe the buried interface roughness. Various groups have carried out experiments to study the influence of micro-roughness on SHG from different material systems, such as Si/SiO_2 system[24-27] and ultra-thin high-k material on a Si substrate[28].

Downer's group carried out the first systematic SHG studies of randomly oriented, angstrom-scale micro-roughness at $Si(100)/SiO_2$ interfaces[27]. As shown in Figure 2.1, the top two panels show the rotational SHG data. The bottom panel shows the corresponding AFM images. The results clearly show that in the *p-p* configuration SHG is highly sensitive to interface micro-roughness. On the other hand, the *s*-polarized SHG

output is unaffected by the surface etching as shown in the middle panel of figure 2.1. The results demonstrate that, contactless and noninvasive SHG technique is a good way to measure the angstrom-level Si/SiO_2 interface roughness.

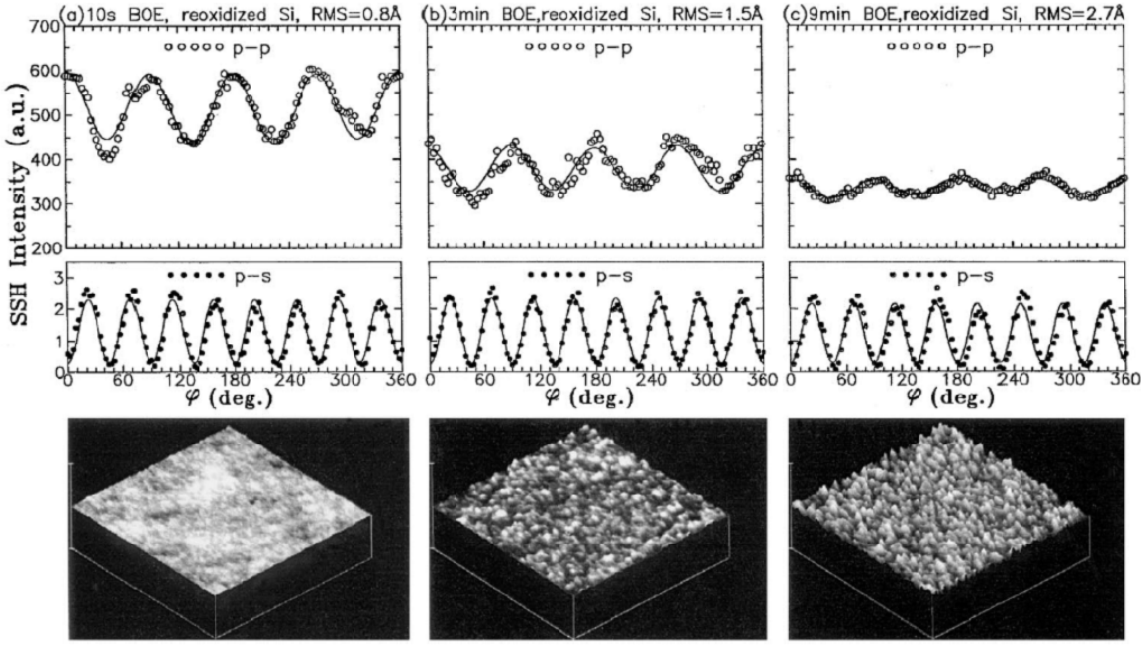

Figure 2.1. Surface SH intensity vs. φ in re-oxidized Si(100), *p-p* configuration (open-circles, top panel), and *p-s* configurations (filled circles, middle panel). The solid lines are the corresponding fits to the data. The corresponding AFM scans in the bottom panel show measured rms (root-mean-square) values of 0.8, 1.5, and 2.7 A, respectively[27].

2.3. Stress relaxation at Si/SiO_2 system monitored by SHG

Microscopically, SHG is generated by the motion of the valence electrons in the asymmetric potential at the interface[20]. Both dangling bonds and distorted bonds caused by interface stress directly lead to SHG. In silicon growth processes, hydrogen terminates the silicon surface dangling bonds and therefore significantly suppresses the

SHG intensity. Many experiments have showed that SHG is an effective *in situ* real time monitoring tool for hydrogen desorption and absorption during silicon growth[29-34].

Various experiments have been done to investigate the effect of interface stress on SHG. Govorkov *et al.* reported using SHG to monitor mechanical stress relaxation at the Si(111)/SiO_2 interface during several annealing cycles[35], where SHG responded differently to different annealing cycles. Daum *et al.* reported SHG resonance caused by the electronic transition of strained Si(111)/SiO_2 and Si(100)/SiO_2 interface layers[36]. Alexandrova *et al.* observed a polar effect, which SHG intensity changes with incident angle, and then proposed the possible origin of the observed SHG pattern is a transitional strained layer of the hydrogen-terminated silicon film close to the substrate[37]. Miyashita *et al*. found that distortion of crystal structure due to residual stress and applied comprehensive stress may be a significant contributor to SHG response[38].

Ito and Hirayama *et al.* reported that the SHG signal from Si(111)/SiO_2 was reduced after hydrogen annealing, while it didn't change after the nitrogen annealing[39]. The wafers examined were boron-doped, 1.3-3 $\Omega \cdot cm$ Si(111) with 500-$\mathring{A}$-thick thermally grown oxide layers. Samples were annealed at 430 $^{\circ}C$ in either a hydrogen or a nitrogen atmosphere.

The *s*-in/*p*-out SH intensity is described as[40, 41],

$$I_{s,p}^{(2\omega)} \sim | A\chi_{zxx} + B\chi_{xxx} \cos(3\phi) |^2 , \qquad (2.7)$$

where A and B are constants, χ_{zxx} and χ_{xxx} are second-order nonlinear susceptibilities at the interface. Specifically, χ_{zxx} and χ_{xxx} originate from the asymmetry of the local potential, which the valence electron feels, along the interface normal direction and parallel direction, respectively.

Second harmonic generation from these samples were measured and shown in Figure 2.2. The asymmetric rotational dependence of the SHG was observed on the unannealed interface. On the hydrogen annealed interface, the large peaks were reduced greatly and the asymmetry was becoming a quasi-sixfold symmetry. However for the nitrogen annealed interface, the rotational asymmetry was preserved. By fitting the experimental data to the equation, χ_{zxx} and χ_{xxx} were obtained as functions of hydrogen annealing time, shown in Figure 2.3 (a), and of nitrogen annealing time, shown in Figure 2.3 (b).

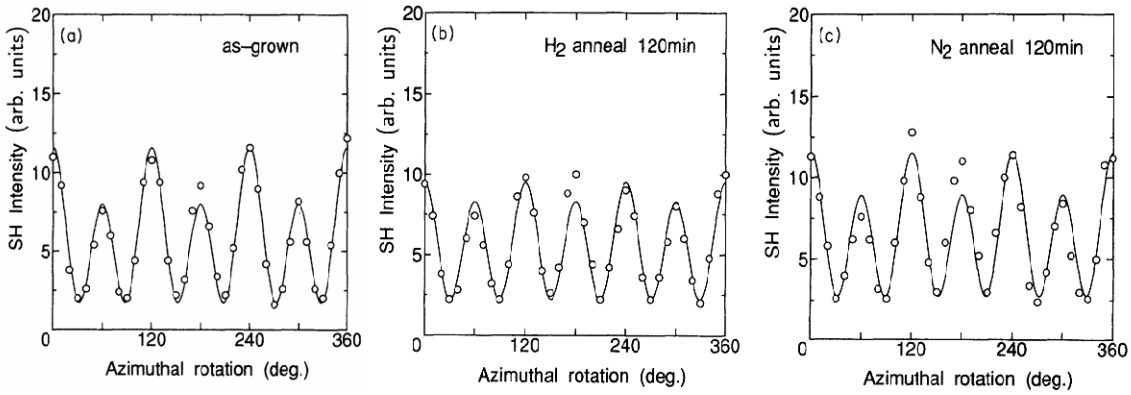

Figure 2.2. Azimuthal rotation dependence of the SH intensity from Si(111)/SiO_2 interfaces which were (a) unannealed, (b) hydrogen annealed for 120 minutes, (c) nitrogen annealed for 120 minutes. Solid curves are the fits using equation (2.8)[39].

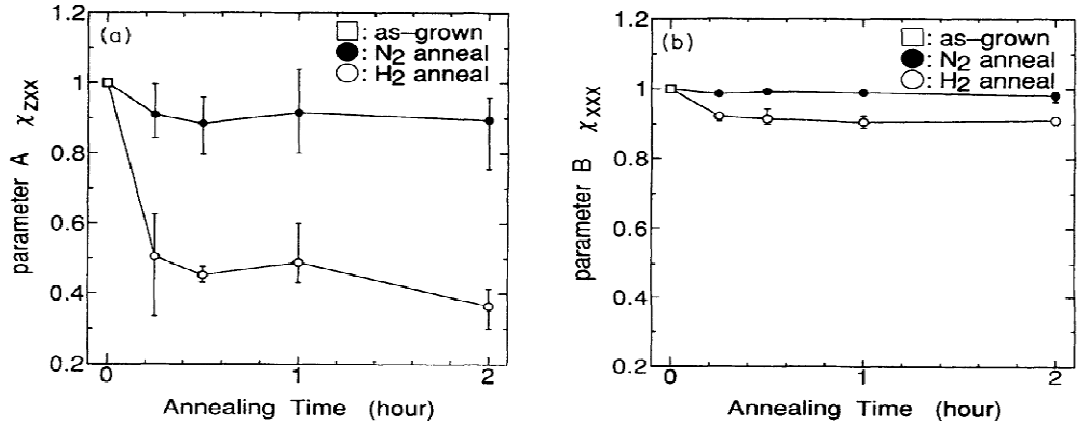

Figure 2.3. Annealing time dependence of (a) χ_{zxx} and (b) χ_{xxx} for hydrogen-annealed and nitrogen-annealed samples[39].

From Figure 2.3, it can be seen that χ_{zxx} is greatly reduced by the hydrogen annealing but only exhibits a slight decrease with the nitrogen annealing , while χ_{xxx} shows a negligible decrease in both annealing processes. The authors concluded that the hydrogen effectively terminates the interface dangling bonds and then reduces the local potential asymmetry along the interface normal direction. The decrease of the nonlinear susceptibility tensor component χ_{zxx} correlated with the reduction in the interface state density of the dangling bonds and therefore caused the reduction in SHG.

2.4. Summary

The properties of the Si/SiO2 system form the basis of much of the semiconductor industry, and are therefore the subject of intensive research. Because second harmonic generation is very sensitive to interfaces and probes the material contactlessly and

noninvasively, much work has been carried out applying second harmonic generation to study Si/SiO_2 interfaces. In this chapter, we have reviewed some significant experiments from other groups.

CHAPTER Ⅲ

ELECTRIC FIELD INDUCED SECOND HARMONIC GENERATION (EFISH), BACKGROUND

3.1. Introduction

Electric-field induced second harmonic generation (EFISH) arising from internal photoemission is being increasingly used for fundamental studies of charge carrier dynamics in semiconductor/insulator systems[7-9]. Wavelength-dependent EFISH measurements can identify and measure thresholds in multi-photon carrier injection processes, which make it possible to obtain band offsets and defect trap levels[42, 43]. These indicate that one may be able to use the contactless and non-invasive SHG technique as an alternative to conventional electrical measurements for *in-situ* monitoring of the properties of thin dielectric layers. In this chapter, we will discuss previous work associated with EFISH.

An incoming optical field causes the electrons in a material to oscillate resulting not only in a linear polarization but also higher order polarizations. Depending on the material symmetry, the oscillatory response in turn results in the generation of light of the same wavelength as well as second- and higher order harmonic signals. The addition of a separate non-oscillatory field which modifies the local electron potential, also causes a second order nonlinear polarization which can be expressed as

$$P_{add}^{(2)}(2\omega) = \chi^{(3)} E(\omega) E(\omega) E(add) \tag{3.1}$$

$\chi^{(3)}$ is a fourth-rank tensor describing the third-order nonlinear susceptibility of the material. It represents the coupling between the electric field produced by the incident light $E(\omega)$ and the field present at the interface $E(add)$.

$P_{add}^{(2)}$ includes polarization from the interface and the bulk. In most of our experiments, the material used is Si/SiO_2. The bulk oxide third-order susceptibility is about 10^4 smaller than for bulk Si[44]. Also, the interfacial electric field is restricted within the interfacial region. Thus, the $P_{add}^{(2)}$ is mainly from the Si interface since in our case, there is no electric field other than the optical field in the Si bulk.

The total second-order nonlinear polarization arising from the Si/SiO_2 interface can be expressed as

$$P_{tot}^{(2)}(2\omega) = \chi^{(2)} E(\omega) E(\omega) + \chi^{(3)} E(\omega) E(\omega) E(add) = (\chi^{(2)} + \chi^{(3)} E(add)) E(\omega) E(\omega) \tag{3.2}$$

Hence, with the presence of an additional field, the total SH intensity can be written as

$$I^{(2\omega)} = | \chi^{(2)} + \chi^{(3)} E(add) |^2 \ (I^{(\omega)})^2 \ , \tag{3.3}$$

where *E(add)* can be externally applied field *E(ext)*, intrinsic field *E(int)* or slowly time-varying photo-induced electric field *E(t),* depending on the material and the experimental configuration. $\chi^{(2)}$ and $\chi^{(3)}$ both describe the response of the interface.

Another way to look at the SHG response, is that in the presence of a non-oscillatory electric field $E_l(dc)$, the bulk inversion symmetry is broken and the contribution to the nonlinear polarization from both the Si and oxide bulk is allowed. In this case, the second-order polarization density can be described as[44, 45],

$$P(2\omega) = P^{SD}(2\omega) + P^{BD}(2\omega) + P^{BQ}(2\omega) \ , \tag{3.4}$$

where $P^{SD}(2\omega)$ is the surface nonlinear polarization, $P^{BD}(2\omega)$ is the bulk dipole electric field induced polarization, and $P^{BQ}(2\omega)$ is the bulk quadrupole contribution.

The surface dipole contribution is given by equation (1.5) as [$P_i^{(2)}(2\omega) = \sum_{jk} \chi_{ijk}^{(2)}(2\omega, \omega, \omega) E_j(\omega) E_k(\omega)$] and the bulk dipole electric field induced polarization is given by

$$P^{BD}(2\omega) = \chi_{ijkl}^{(3)} E_j(\omega) E_k(\omega) E_l(dc) \ . \tag{3.5}$$

The bulk quadrupole contribution is given by

$$P^{BQ}(2\omega) = \Gamma_{ijkl}(2\omega : \omega, \omega, \omega) : E_j(\omega)\nabla_k E_l(\omega)\,, \tag{3.6}$$

where Γ_{ijkl} is a fourth-rank tensor which describes the quadrupole contribution to the quadratic nonlinear susceptibility from spatial dispersion. It has the same symmetry properties as $\chi^{(3)}_{ijkl}$ in equation (3.5).

Therefore, the total second harmonic generation signal may be a superposition of signal from the bulk quadrupole, the surface dipole, and EFISH. Since in our case there is no slowly varying electric field in the bulk Si, there is no contribution from this source. However, there may be a very small contribution from the oxide bulk due to the fact that a slowly varying field is present. Clearly however, the EFISH contribution to the nonlinear polarization can easily exceed those from other sources. We should note that an EFISH signal can be created either by applying an external bias to the material or by photo-inducing a charge separation across the interface as done in our experiments. In most semiconductor structures, there is a built-in electric field due to charges trapped at the defect centers or trap sites at the interface. The most prominent defect in the interfacial region of a Si/SiO_2 system is the P_b center[46]. It is a dangling bond defect where a Si atom is bound to three other Si atoms. Other types of defects at the interface are impurity defects, which is due to passivation of broken bonds at the interface by impurities such as H or Cl.

3.2. Photo-excitation at Si/SiO_2 interfaces

EFISH research by van Driel's group on photo-excitation at the Si/SiO_2 interfaces has shown the important role of electrons in the creation of the interface electric field[44, 47-51]. Van Driel *et al.* showed that the time-dependent second harmonic generation (TD-SHG) intensity increases rapidly as a fundamental beam irradiates the Si/SiO_2 interface and then gradually saturates[47, 48]. Figure 3.1 shows a typical TD-SHG curve from a $Si(100)/SiO_2$ surface[47].

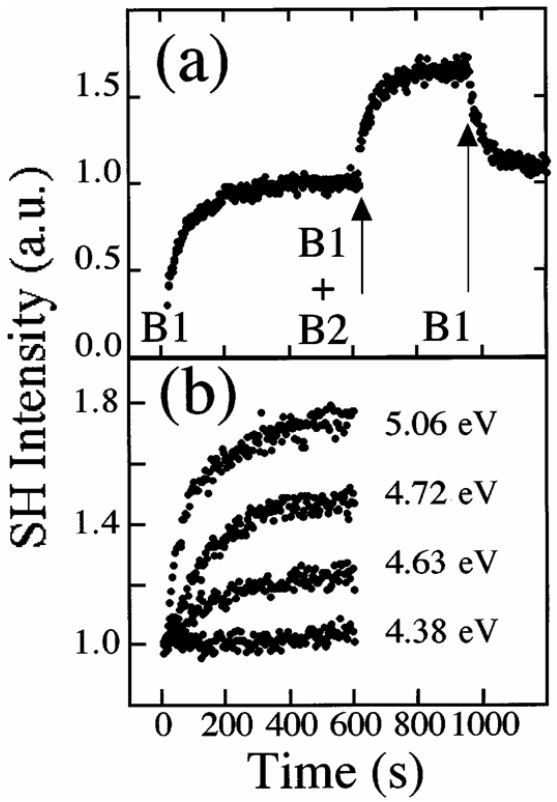

Figure 3.1. SHG from an oxidized *n*-Si(001) sample illuminated laser pulses at an angle of incidence of 80° (a) at average irradiance of 1.3 $kWcm^{-2}$ (beam B1), with a second 3.6 $kWcm^{-2}$ (beam B2) at normal incidence; and (b) at average irradiance of 0.5 $kWcm^{-2}$, with a normal incidence ultraviolet beam at the photon energies indicated[47].

When electrons are injected from the silicon valence band into the SiO_2 conduction band, they are trapped mainly on the oxide external surface while the holes remain primarily in the silicon valence band near the interface. The resulting charge separation accounts for the photo-induced electric field. The degree of charge separation determines the interface photo-induced electric field $E(t)$ and therefore affects the TD-SHG signal.

The TD-SHG signal can be characterized by equation (3.3), where *E(add)* now is *E(t)*, the time-varying photo-induced electric field across the interface. It is clear that the observed $I^{(2\omega)}$ depends on the interface nonlinear susceptibility and also the charge-separation-induced electric field at the interface.

Previous experiments have reported that the ambient oxygen facilitates the trapping of the photo-injected electrons at the oxide surface. Van Driel's group found that the oxygen molecules capture the electrons at the surface of the oxide due to the high electron affinity of oxygen molecules[47, 52]. It has been shown that the saturated EFISH intensity varies with the oxygen pressure and also the oxide thickness, as in figure 3.2 and 3.3, respectively.

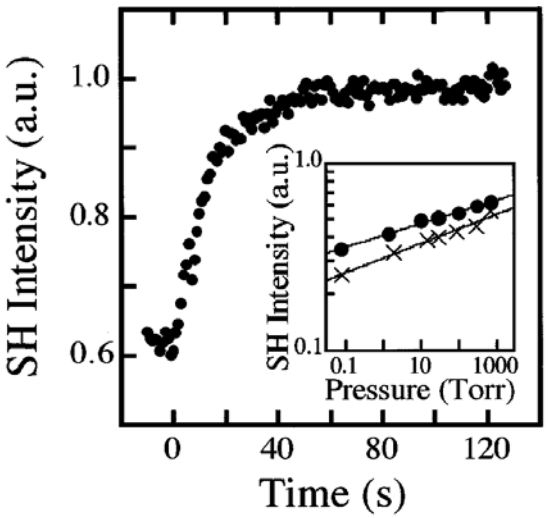

Figure 3.2. SHG signal observed from oxidized *n*-Si(100) after the ambient oxygen pressure is increased from 10^{-2} to 760 Torr in 2 s. The inset shows the pressure dependence of the steady-state SHG intensity for increasing (crosses) and decreasing (circles) pressure. The data sets are offset for clarity[47].

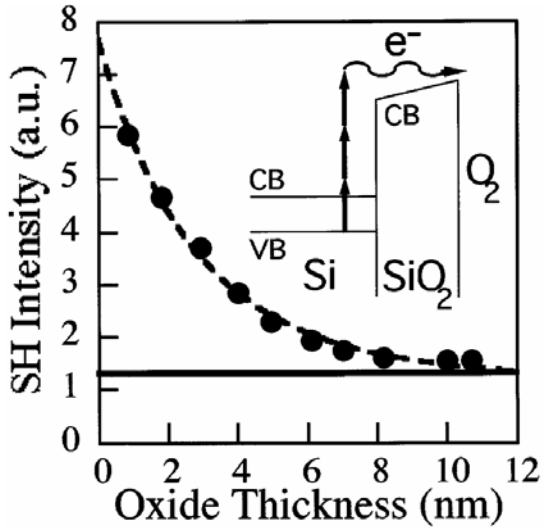

Figure 3.3. Oxide thickness dependence of the steady-state SHG from *p*-Si(100) for constant irradiance of 0.25 kW cm^{-2} at an angle of incidence of 45° . The horizontal line indicates the quiescent level observed for all samples. The inset shows a schematic diagram of a possible electron excitation or transfer process[47].

The saturation level of EFISH signal decreases while the ambient oxygen pressure decreases and eventually vanishes around 10^{-10} Torr[47], as shown in Figure 3.2. The EFISH intensity varies with the oxygen pressure because the number of available electronic trap states changes with the density of oxygen molecules at the surface which itself varies with oxygen pressure.

The thickness dependence of EFISH signal shows that for oxides thicker than ~ 10 nm the signal could not be observed[47], as shown in Figure 3.3. Van Driel *et al.* concluded that the low signal is because of the scattering effects. It is worth pointing out that, the scattering length of electrons in the oxide is about 3.4 nm[53]. Scattered electrons would be preferentially redirected back to the positively charged silicon before being captured by oxygen.

3.3. Photo-induced EFISH in a $Si/(ZrO)_x(SiO_2)_{1-x}$ structure

Previous work in our group done by Glinka *et al.* used the photo-induced EFISH technique to monitor a $Si/(ZrO)_x(SiO_2)_{1-x}$ system[9]. Figure 3.4 shows TD-EFISH signal from a sample. An interesting feature can be observed from this figure: when the laser intensity is relatively low (less than 400 mW), the EFISH signal decreases at the instant when the laser irradiation is applied.

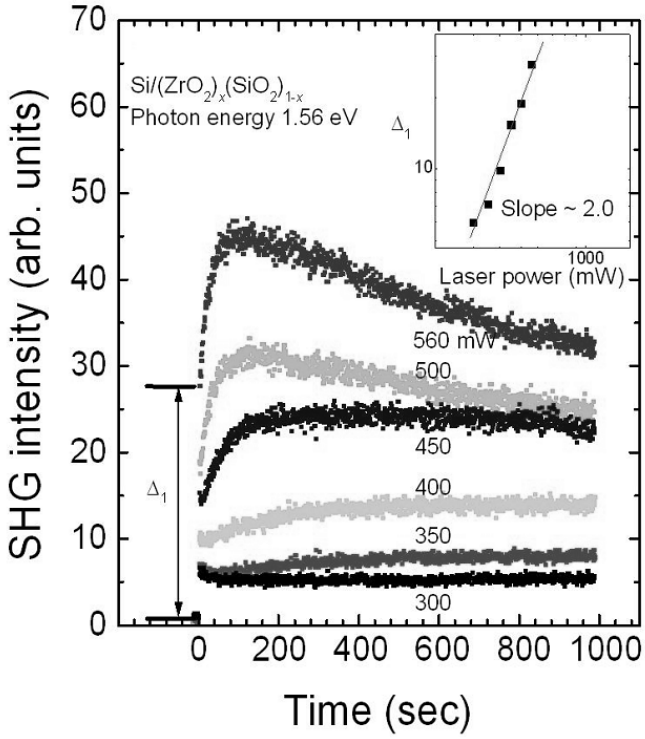

Figure 3.4. EFISH signal from the interface of $Si/(ZrO)_x(SiO_2)_{1-x}$. The photon energy is 1.56 eV. The laser power varies between 300 and 560 mW. The inset shows the dependence of the SHG signal at t = 0 *vs.* laser power on a log-log scale[9].

The authors suggested that the initial decrease in the signal is related to the fact that there is an initial dipole field at the interface, which is also supported by previous nonoptical measurements at the $Si/(ZrO)_x(SiO_2)_{1-x}$ interface[54]. The charges accumulated near the interface are negative in silicon and positive in the oxide. Therefore, the initial interfacial electric field is directed toward the silicon substrate. As electrons are injected, an electric field in the opposite direction, due to charge separation, begins to develop. This results in a decreasing net field. The net field decreases to a minimum and then begins to increase, in the direction opposite to the initial interfacial electric field. This feature occurs due to an interplay between the initial dipole static field E_0 and the TD photo-induced electric

field *E(t)* at the interface caused by the injection and trapping of charge carriers in the oxide. A cross-term in the equation shown below adequately describes this behavior,

$$I^{(2\omega)} = |\chi^{(2)} + \chi^{(3)}(E_0 - E(t))|^2 \, (I^{(\omega)})^2 . \quad (3.7)$$

3.4. Photo-induced EFISH as a technique for measuring band-offsets

Another optical application based on EFISH carried out in our group is a 'two-color experiment' developed by Marka *et al.* to measure the band offsets at semiconductor interfaces[43]. The 'two-color technique' is described in detail in chapter IV.

Marka *et al.* used a tunable optical parametric generator (OPG), as a pump laser source, to inject carriers at different powers and photon energies, and a Ti:sapphire laser at low intensity, as a probe laser source, to monitor the TD-electric field via SHG. From power dependent EFISH measurements, the number of photons required to excite electrons from silicon valance band to the SiO_2 conduction band could be found.

The number of photons required to inject an electron from silicon to SiO_2 was determined for several different energies in a range of pump photon energies (1.9 – 4.8 eV), as shown in Figure 3.5.

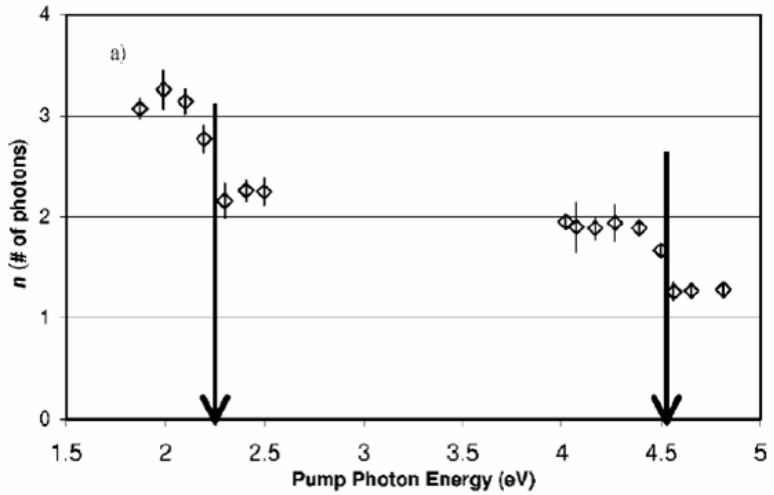

Figure 3.5. The order of electron injection process from Si into SiO_2 *vs.* the photon energy of the pump beam, determined from the intensity dependence of injection rates[43].

The stepwise jumps from one- to two-photon (between 4.56 and 4.50 eV) and then from two- to three-photon (between 2.30 and 2.20 eV) processes, as the incident pump energy decreases, were observed. The energies for stepwise jumps were identified as the thresholds for one-photon (~ 4.53 eV) and two-photon (~ 2.25 eV) electron injection from the Si valence band into the SiO_2 conduction band. These results were in good agreement with other band offsets measurements and theoretical predictions, which vary in the 4.05 – 4.6 eV range[55, 56]. This was the first time that multiphoton internal photoemission thresholds were observed.

3.5. Charge trapping in irradiated SOI wafers measured by SHG

The work on SOI wafer by Jun *et al*. in the Vanderbilt group showed that, photo-induced SHG provides information about charge carrier dynamics in SOI structures, defect buildup and annealing rates[8].

The SOI wafers used in the experiment were UNIBOND wafers. The SHG test was performed using a Ti:sapphire laser at wavelength of 800 nm with average power of 600-730 mW. The sample wafer was defined with three different regions containing different interface(s) and the detected SHG intensity from different regions included effects from different interface(s).

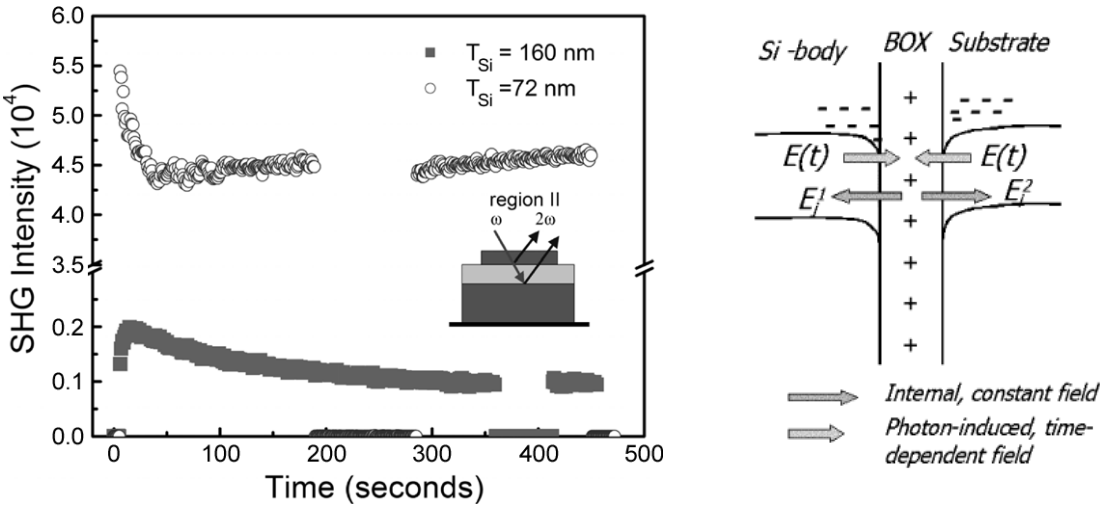

Figure 3.6. (Left) Examples of SHG signals from region II of samples with BOX thickness of T_{Si} = 145 nm and 230 nm. Inset shows Region II which contains two interfaces (Si film/BOX and BOX/substrate). (Right) Schematic energy band diagrams of Si/BOX/substrate regions[8].

Figure 3.6 (Left) shows SHG signals from region II with different Si island thicknesses. For the thicker Si island wafer, the SHG signal is smaller due to absorption in the thick Si. Figure 3.6 (Right) shows the optically-generated charge separation at both interfaces. The charge separation produces a time-dependent electric field *E(t)* compensates the initial fields, E_i^1, E_i^2, from the residual positive charges after the wafer process. (Typically, a UNIBOND wafer contains residual positive charges in the BOX, which makes the flatband voltage negative.)

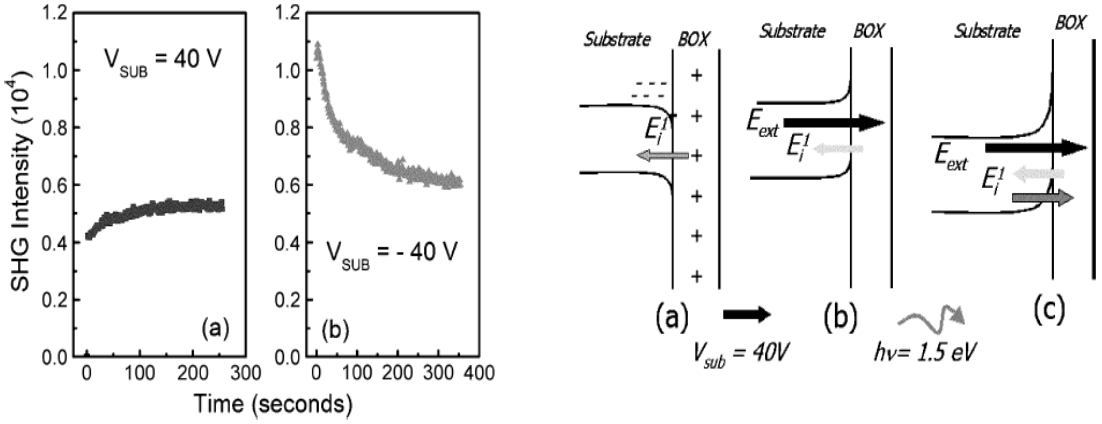

Figure 3.7. (Left) Examples of SHG signals with an external bias applied to the substrate prior to the laser beam illumination; (a) 40 V on the substrate and (b) – 40 V on the substrate. (Right) Schematic energy band diagrams of substrate/BOX regions. In (b) and (c), the internal fields are compensated and illustrated as light gray. The dark grey indicates the electric field due to charge separation[8].

A positive bias was applied to the substrate to study the bias effect on SHG intensity. The charge redistribution at the interface between the substrate and the BOX due to the external field is illustrated in figure 3.7 (Right). (a) shows the interfacial field created by

the oxide charges and is compensated by the externally field applied field, as shown in (b). (c) shows the net field increases due to the charge separation. Figure 3.7 (Left) shows SHG signals with substrate biases of 40 V and – 40 V. It is evident that both time-independent and time-dependent interfacial fields are strongly affected by the external fields across the oxide. Moreover, the initial SHG intensity at t = 0 with negative bias – 40 V is more than twice large than that with a positive bias 40 V. This implies that the bottom interface creates a larger time-independent electric field than the top interface after the external field is applied across the structure.

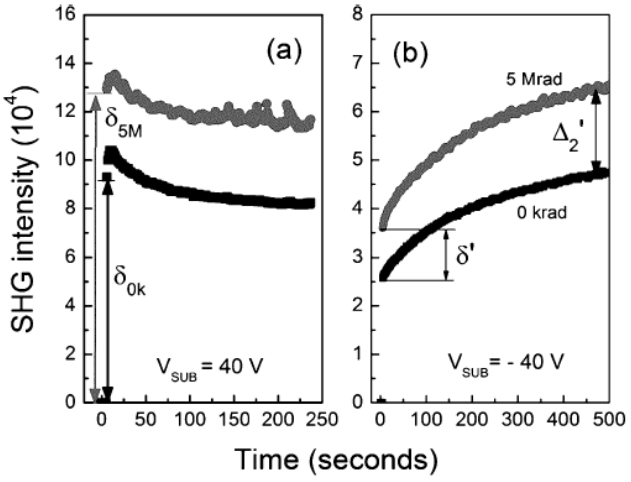

Figure 3.8. Example of SHG signals versus substrate bias before and after the total dose of 5 Mrad. T_{Si} = 72 nm and T_{BOX} = 230 nm[8].

Radiation-induced charge can change the charge distribution in the Si, which directly affects the local fields at the interfaces. Figure 3.8 shows the SHG signals from region II of a sample at a total dose of 5 Mrad. Both the initial and saturation levels of the SH

intensities increase regardless of the applied bias, indicating that radiation-induced trapped charges increase the local fields at the interfaces.

3.6. Summary

Electric field induced second harmonic (EFISH) generation has proven to be a sensitive probe of electron transfer in the Si/SiO_2 system. In this chapter, we review some significant research associated with EFISH from other groups. We also introduced the application of the novel 'two-color' SHG technique by Marka *et al*. and the work on SOI wafers by Jun *et al.* from our group.

CHAPTER Ⅳ

EXPERIMENT CONFIGURATION

4.1. Introduction

The invention of the wavelength tunable Ti:sapphire laser enabled a large class of ultra-fast experiments not previously possible, including many second harmonic generation experiments. The work presented here is carried out employing a Ti:sapphire laser at wavelength of 800 nm. We also use a novel 'two-color' technique using a combination of Ti:sapphire and optical parametric generator (OPG) lasers, which enables us to separate the charge carrier injection from second harmonic generation. In this chapter, we will take a historical and scientific look at the Ti:sapphire laser and then describe the conventional 'one-beam' technique and the novel 'two-color' technique used in our experiments.

4.2. Ti:sapphire laser

Before the year of 1986, mostly dye lasers dominated the fields of ultrashort pulse generation and widely wavelength-tunable lasers. A dye laser is a laser based on a dye (in a liquid solution or in solid form) as the gain medium, which is radically different from other types of lasers. A wide range of emission wavelengths from the ultraviolet to the near infrared region can be addressed with different laser dyes[57]. However dye lasers

are difficult to operate and maintain. Alternatively, another type of laser, broad-bandwidth solid-state lasers, was developed. In 1982, Peter Moulton of MIT Lincoln Labs first discovered the titanium sapphire (Ti:sapphire) laser. It took six years, until 1988, for the Ti:sapphire laser to be introduced commercially and where it quickly replaced most dye lasers. The production of the Ti:sapphire laser was driven by the need for an ultra-fast laser with a relatively large wavelength range.

The Ti:sapphire laser is a common solid-state laser. Solid-state lasers have a metal ion embedded in a transparent crystal or glass as the gain medium. In the case of a Ti:sapphire laser, the gain medium is titanium-doped sapphire (Ti^{3+}:sapphire). Sapphire has an excellent thermal conductivity, alleviating thermal effects even for high laser powers and intensities. The Ti^{3+} ion has a very large gain bandwidth, allowing the generation of very short pulses as well as wide wavelength tunability.

In late 1989, a group at MIT reported 200 femtosecond pulses generated from a Ti:sapphire laser[58]. They used a novel mode-locking technique called *additive pulse mode-locking* (APM). The APM is accomplished by feeding back into the laser part of its output after it has been nonlinearly modulated in an external cavity. Spence *et al.* at the University of St. Andrews reported that they observed *self-mode-locking* or *Kerr lens mode-locking (KLM)* of a Ti:sapphire laser[59]. This type of mode-locking is induced in a solid-state laser because the nonlinearity is present in the laser crystal.

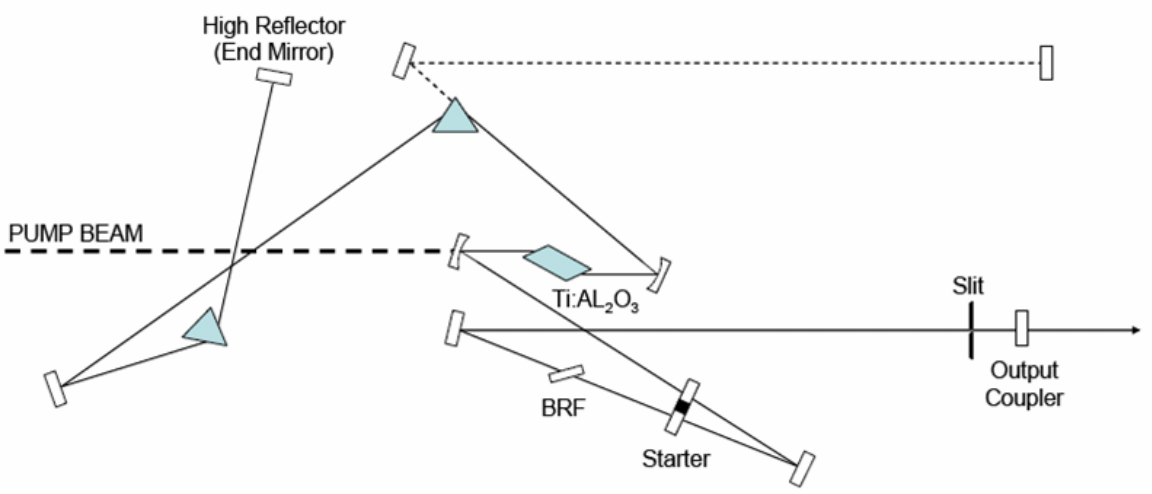

Figure 4.1. The schematic diagram of a typical self mode-locked Ti:sapphire laser[60].

The laser used in the experiments reported in this thesis is the Coherent Mira 900. Figure 4.1 shows a schematic diagram of a typical self mode-locked Ti:sapphire laser cavity[60]. The Mira laser operates on the KLM technique. In the KLM process, the optical cavity is specifically designed to optimize mode-locking by utilizing changes in the spatial profile of the beam. These changes are produced by the self-focusing that results from the optical Kerr effect in the Ti:sapphire crystal. The process itself is initiated by a simple, optical design that varies the cavity length to create transient short-pulse fluctuations. KLM is a highly reliable, all-solid-state mode-locking technique that requires no unnecessary, additional cavity elements such as an acousto-optic modulator, and is analogous to a fast saturable absorber. The result is the efficient generation of short pulses in either the femtosecond or picosecond regime.

The Coherent Mira 900 laser has a wide wavelength tunability, which is 720 to 900 nm. The pulse energy is ~ 10 mJ, repetition rate is ~ 76 MHz, and pulse width is ~ 150 fs. It is pumped by a stable 5-W Verdi diode-pumped 532 nm green laser.

4.3. The One-beam SHG technique

The simplest and most widely used SHG technique is the detection of the reflection of optical SHG. In most of SHG experiments, laser pulses of frequency ω are incident on surfaces of the material system at an angle $\theta < 90^0$ and SHG pulses of frequency 2ω are generated in reflection. Figure 4.2 shows the conventional setup for a single-beam SHG experiment.

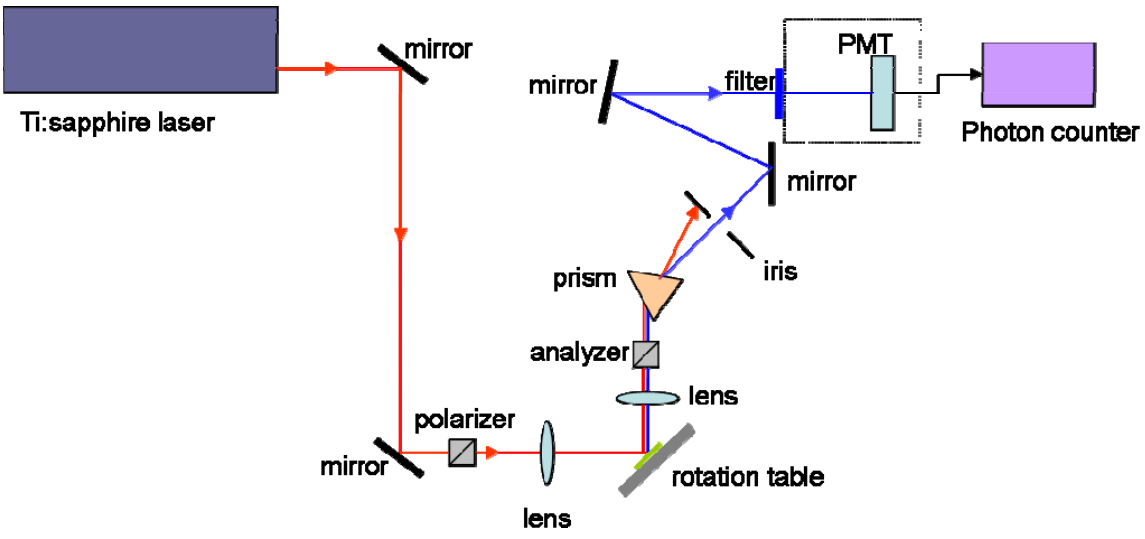

Figure 4.2. The schematic diagram of a single-beam SHG setup.

The sample is placed on an aluminum plate, which acts as a heat sink to reduce the local heating. The fundamental laser beam is directed to the sample at a non-normal incident angle, which in most cases is 45º. A prism is to optically separate the fundamental and second harmonic beams. The second harmonic beam is then collected and focused by lenses and detected by a photo-multiplier tube and measured by a photon counter. A typical spot diameter on the sample is in the neighborhood of a few tens of micrometers. The polarizer and the analyzer are to change the polarizations of the fundamental and the second harmonic beams, providing the ability for different system configuration. Additional irises and filters are applied to further reduce the fundamental beam reaching the detector. The rotation table allows us to change the azimuthal angle and perform the angular dependence measurements.

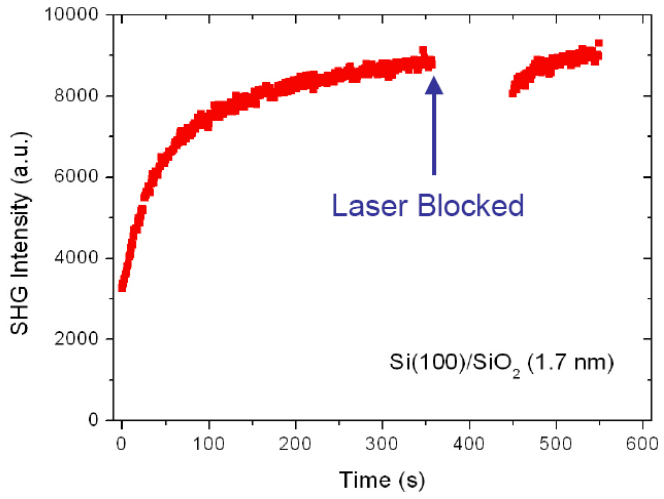

Figure 4.3. A typical TD-EFISH measurement from a Si(100)/SiO_2 sample. The top layer is thermally grown 1.7 nm SiO_2.

Figure 4.3 shows typical time-dependent EFISH data from a Si/SiO_2 system. The top oxide layer thickness is 1.7 nm thermally grown on silicon (100). As shown in the figure, at t = 0 s when laser is directed onto the sample, SHG intensity starts at some nonzero level, which is the second-order nonlinear susceptibility response from the interface. As the laser irradiate on the sample, the SHG intensity increases. The increase of the SHG intensity is the result of the charge separation and subsequent electron trapping at the interface and/or the surface of the oxide. Gradually the SHG saturation is reached and the laser is blocked manually by putting a blocker in the beam path. This is the so-called 'dark time'. After about 100 s of dark time, the laser is unblocked. The SHG intensity starts at a level lower than before the laser is blocked. This observation can be explained by quantum tunneling of electrons from the oxide surface back to the interface through the ultrathin oxide and recombine with the holes, which reduces the electric field across the interface and subsequently reduces the SHG intensity.

The single-beam SHG technique is widely used because it is simple and easy to setup. In this setup, the laser beam is used for two purposes. First, it creates the electron-hole pairs via a single/multi-photon process, which allows the electrons to be injected into the oxide. Second, an interfacial electric field created by the charge separation can be detected by the same laser source. In next section, we will introduce a new technique, two-color SHG technique, which enables us to separate the monitoring of SHG and creation of the photo-induced electric field.

4.4. The two-color SHG technique

In most of the previous TD-SHG experiments, a single laser source is used, which serves two purposes, creation of photo-induced electric field and monitoring the electric-field induced second harmonic signal.

In the two-color EFISH technique, developed by Marka *et al.*, two separate tunable lasers are employed. The first laser operating in the visible and UV, with relatively high intensity, serves to optically pump electrons into the oxide. The injection and trapping of electrons create an interface electric field. The second laser operating in the near IR probes the resulting electric field by measuring the EFISH signal. The intensity of the probe beam is intentionally lowered so that it doesn't contribute to the charge separation and accumulation. The pump and probe functions are separated in this way (as seen in Figure 4.4).

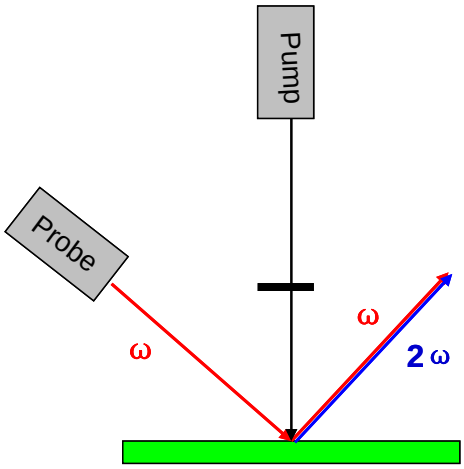

Figure 4.4. Schematic diagram of the two-color SHG technique.

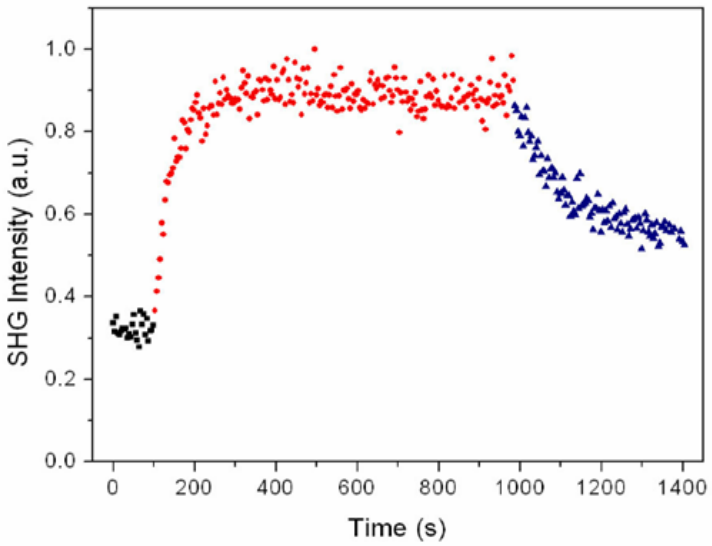

Figure 4.5. Typical TP-EFISH response from the Si(100)/SiO_2 system with two-color technique. Oxide layer thickness is 1.7 nm.

Figure 4.5 presents a typical TP-EFISH response from the ultrathin Si(100)/SiO_2 using the two-color technique. Three stages are observed in the figure. At the first stage, only the probe laser is on, which allows recording the SHG intensity only due to the second-order nonlinear susceptibility without any significant charge accumulation. During the second stage of the experiment, both pump and probe lasers are on. The high intensity pump laser beam injects electrons from silicon valence band to oxide conduction band via single/multi-photon excitation process. The electrons subsequently transport and get trapped at the oxide surface. The charge separation creates an interfacial electric field. The probe laser beam detects and records an increased SHG signal induced by this interfacial electric field. During the third stage, the pump beam is switched off and the probe beam detects the decreased SHG signal due to the recombination of the electron-hole pairs.

4.5. Summary

In this chapter, we examine the history and the technical features of the Ti:sapphire laser. We also describe the experimental setup and SHG techniques used in our work. The novel ‘two-color’ laser technique enables us to experimentally separate the detection of SHG and the carrier injection processes and then directly follow the photo-induced charge carrier dynamics.

CHAPTER Ⅴ

SECOND HARMONIC GENERATION FROM SILICON-ON-INSULATOR (SOI) STRUCTURES

5.1. Introduction

Previous work by Jun *et al.* on silicon-on-insulator (SOI) done in Vanderbilt group has shown that second harmonic generation effectively detects the increase of the interface field due to the radiation-induced oxide and interface traps[8]. In this chapter, we will report our recent work on SOI wafers, which are intentionally contaminated.

The invention of the integrated circuits (IC) in late 1950s by Jack Kilby (late July 1958, in Texas) and Robert Royce (January 1959, in California) showed that multiple transistors could be made in the same piece of Si by isolating neighboring devices from each other with reverse biased *p*-*n* junctions. It was a fundamental breakthrough in technology. Silicon dioxide has been the exclusive choice as a gate dielectric for semiconductor devices since the metal-oxide semiconductors (MOS) were introduced in the 1960s. However, today's demanding technology asks for size reduction of the oxide layer on the silicon, which imposes some fundamental limitations on the further use of SiO_2. When the SiO_2 thickness reaches 2 nm, the gate leakage of the metal oxide semiconductor field effect transistor (MOSFET) becomes extremely high. But according to the prediction of technology roadmaps, the SiO_2 gate dielectrics thickness would

diminish below 2 nm. This makes SiO_2 no longer able to meet the technological requirements.

Several approaches have been tried to improve device performance, especially to reduce the unwanted tunneling current[61]. One of the approaches is crystalline oxides on silicon (COS), which can drastically change the scaling laws for silicon-based transistor technology[62]. Silicon-on-insulator (SOI) device structure is another approach pursued by researchers. **M**OS transistors fabricated on SOI wafers have received much attention because of advantages in device isolation, speed, density, and scalability over bulk silicon devices[63].

About 40 years after the invention of the IC, the first implementation of SOI was announced by IBM in August 1998, which according to IBM engineers, 'will accelerate the industry's constant drive to create smaller, more powerful, less expensive electronic goods.' Silicon-on-insulator technology refers to the use of a layered silicon-insulator-silicon substrate in place of conventional silicon substrates in semiconductor manufacturing, especially microelectronics, to reduce parasitic device capacitance and thereby improve performance[64]. The implementation of SOI technology is one of several manufacturing strategies employed to meet the downsizing requirement in semiconductor devices.

5.2. SOI structures characterized and monitored by SHG

Since 1998, the commercial application of SOI has grown exponentially. Benefits of SOI circuits relative to conventional circuits include: enhanced performance (such as high speed, low noise, low power dissipation, reduced short channel effects, and elimination of latch-up) and also extended scalability. From a manufacturing perspective, SOI substrates are compatible with most conventional fabrication processes. Generally an SOI-based process may be implemented without special equipment or significant retooling of an existing factory. Among challenges unique to SOI are novel metrology requirements to account for the buried oxide layer and concerns about differential stress in the topmost silicon layer. The use of non-destructive, non-invasive optical second harmonic generation promises to be able to meet these needs. The SHG process is very sensitive to characteristics of heterointerfaces, which makes the technique well suited to layered material structures such as gate-dielectric to semiconductor interfaces and SOI structures. SHG has been previously investigated to detect defects in the SOI structure and to measure the bias dependence of the SHG signal in SOI wafers[65], and the radiation-induced effects on SOI wafers[8].

It is known that, in SOI wafers, metals may be introduced during wafer fabrication and can be gettered to the Si/BOX interface(s)[66-69]. Subsequent thermal processing may cause the metals to migrate and degrade device yield and reliability. Metal contamination is clearly the interest of SOI wafer manufacturing[70]. The buried oxide (BOX) layer and associated interfaces with the silicon device layer and the substrate in SOI structures are

currently characterized using invasive physical measurements such as atomic force microscopy (AFM) measurements after removal of the top silicon layer by selective chemical etching. Sub-surface contamination in SOI wafers is measured by time-consuming destructive analysis such as secondary ion mass spectrometry (SIMS) or inductively coupled plasma mass spectrometry (ICPMS) on a sampling basis. SIMS is a very sensitive surface and thin film analysis technique used for the characterization of trace and major elements on solid surfaces. However, these conventional techniques all have to contact material surfaces in order to make the measurements. SHG has been demonstrated as a non-invasive, contactless, real-time method to probe semiconductor–insulator interfaces, and is well suited to characterization of properties of SOI wafers[8, 71-73]. Our work demonstrates the potential to apply SHG to non-destructive, non-invasive characterization of SOI wafers.

5.3. Fabrication of SOI Wafers

There are several methods to produce an SOI structure which are generally described by Celler *et al*[64]. Briefly, they are:

1) **Zone Melting Recrystallization (ZMR):** A poly-silicon layer, deposited on the BOX is recrystallized by scanning a laser, e-beam, lamp, or strip heater across the wafer.

2) **Full Isolation by Oxidezed Porous Silicon (FIOPS):** A porous silicon, which is converted from a p-doped silicon wafer by anodic reaction, is rapidly transformed into a BOX during subsequent oxidation.
3) **Separation by IMplantation of OXygen (SIMOX):** SOI wafer is synthesized by internal oxidation during the deep implantation of oxygen ions into a silicon wafer.
4) **Epitaxial Lateral Overgrowth (ELO):** A sigle-crystal silicon film is grown from the substrate through and above the SiO_2 layer.
5) **Wafer Bonding (WB):** An oxidized silicon wafer is mated to a second silicon wafer. After bonding, the top wafer is etched down to reach the target thickness of the silicon film.
6) **UNIBOND:** Wafer bonding is followed by splitting of a thin silicon layer from one of the wafers. The splitting is obtained by deep implantation of hydrogen ions. After bonding and annealing, the wafers separate naturally at a depth defined by the location of hydrogen micro-cavities.

It is almost inevitable that metal contaminations will happen during wafer fabrication. Metal contamination results in the deterioration of the electrical characteristics of the wafer, such as the gate oxide film reliability. Especially with the shrinking of the feature sizes, gate oxide film thicknesses are getting progressively thinner. Even small amounts of heavy metal contamination can cause deterioration in the initial breakdown voltage. Thus, it is essential to detect and evaluate the metal contamination in the SOI wafers during the fabrication. SHG has been proven to be sensitive to the buried layer properties.

Our work on SOI wafers with intentionally introduced metal contaminations illustrates how SHG is a promising tool to detect metal contaminations.

5.4. Sample preparation

In this set of experiments, the SOI wafers used were 100 mm in diameter with BOX and SOI thickness in the 140 – 150 nm and 50 – 85 nm ranges, respectively. The SOI wafers were from Sematech, fabricated using the Separation by IMplanted OXygen (SIMOX) process.

Spot contamination was intentionally introduced onto the back of bonded SOI wafers using Nickel (Ni), Copper (Cu) and Iron (Fe) solutions. The wafers were contaminated with two different concentrations, 10^{12} and 10^{14} cm^{-2}, at different locations on the back, as shown in Figure 5.1. For a comparison, another set of Si/SiO_2 samples were also intentionally contaminated on the back in the same way.

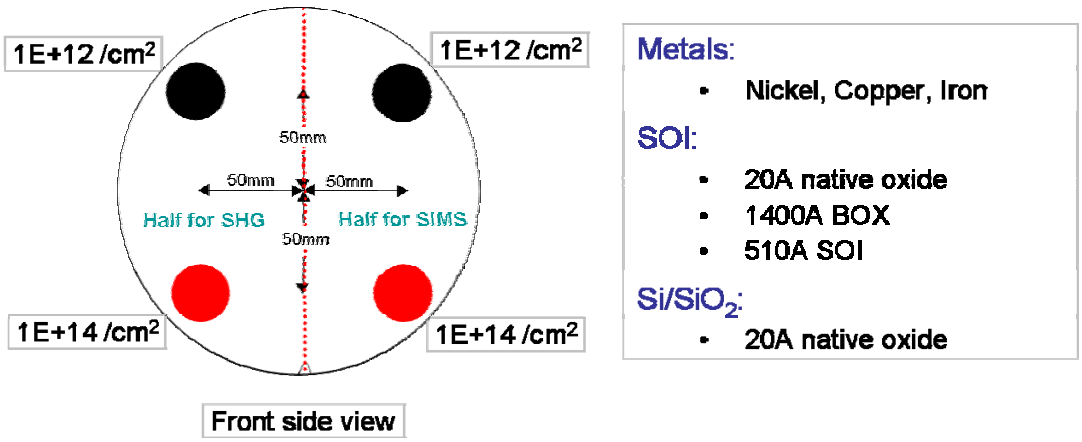

Figure 5.1. (Left) The Schematic front view of wafer showing locations of contamination introduction. Note that contamination was introduced on the back of the wafers in concentrations shown as in solution. (Right) Descriptions of the specifications of the wafer.

After the solutions were allowed to dry, the wafers, including a control wafer with no contamination, were placed in a diffusion furnace for 1 hour at 950°C. Following cooling, wafers were cleaned and characterized by microwave photoconductivity decay (μPCD), as shown in Figure 5.2 for contaminated SOI wafers and Figure 5.3 for contaminated Si/SiO_2 wafers.

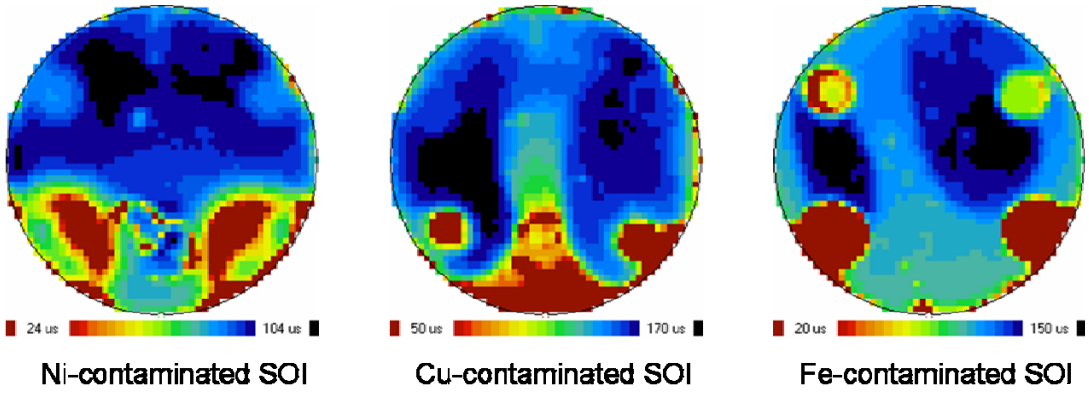

Figure 5.2. Microwave photoconductivity decay (μPCD) images of three SOI wafers with Ni, Cu, Fe contaminations at different locations on the back.

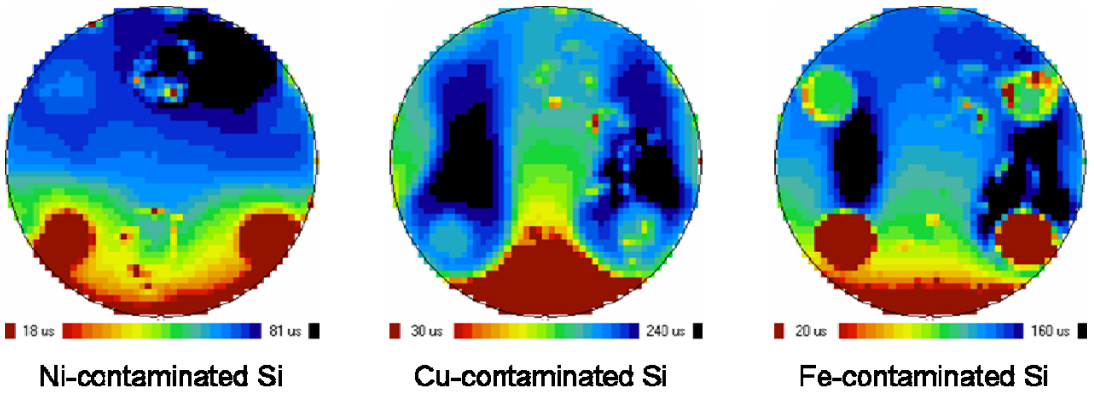

Figure 5.3. Microwave photoconductivity decay (μPCD) images of three Si/SiO_2 wafers with Ni, Cu, Fe contaminations at different locations on the back.

Following the μPCD measurements, wafers were cleaved and half of each measured by SIMS and SHG respectively.

5.5. Experimental setup

The setup for SHG measurement is illustrated in Figure 4.2 in chapter 4 as a typical single-beam SHG setup. An ultrafast femtosecond laser tuned at 800 nm was directed to the sample surface at an incident angle of 45º to generate the SH signal with wavelength of 400 nm. The sample was placed on an aluminum plate to reduce the local heating from the laser beam. A prism was to optically separate reflections of the fundamental beam and the SH beam. A photomultiplier tube is used to detect the SH signal and a gated photon counter is to measure the SH signal.

Figure 5.4 shows the conceptual schematic of the SHG measurement configuration from a SOI wafer. Note that it is assumed that the top native silicon dioxide layer is removed and there are SHG signals coming from the two buried interfaces.

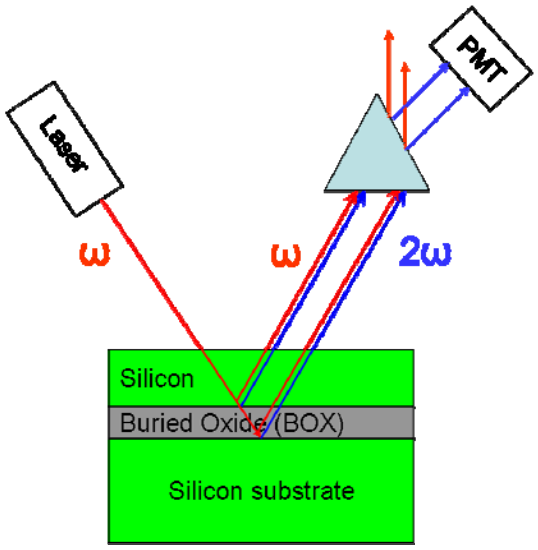

Figure 5.4. Conceptual schematic of the SHG configuration from a SOI wafer after removing the top native oxide layer[74].

5.6. Experimental results and discussions

First, figure 5.5 shows the secondary ion mass spectrometry (SIMS) measurement results for the intentionally contaminated bonded SOI wafers. SIMS is a very sensitive, though destructive, surface and thin film analysis technique used for the characterization of trace and major elements on solid surfaces and can provide the concentration versus depth profile of the material. It is currently widely used to measure the sub-surface

contamination. Measurements were performed on the samples at locations corresponding to the 10^{12} cm^{-2} initial solution concentrations.

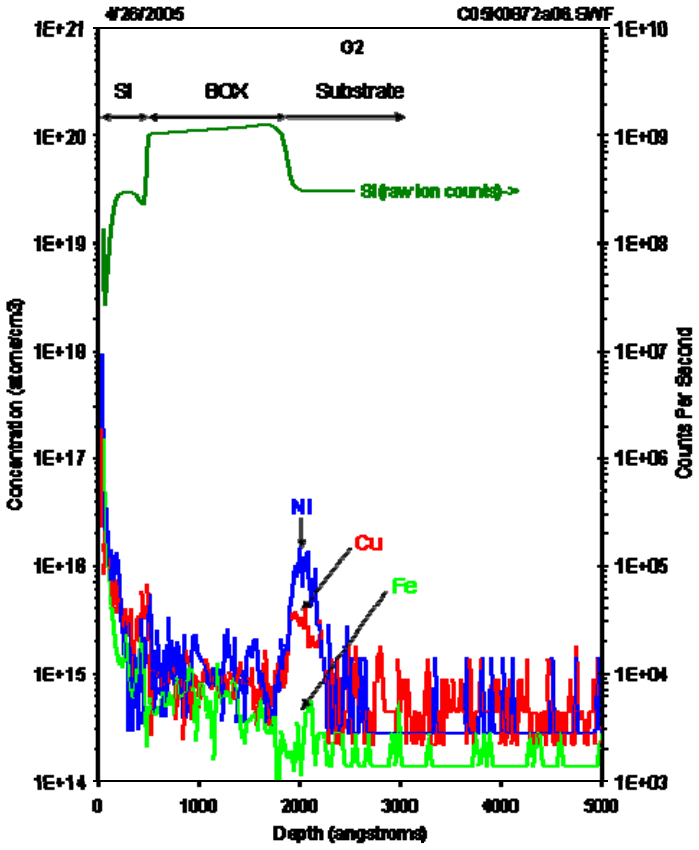

Figure 5.5. SIMS data for intentionally contaminated wafers following the diffusion anneal[74].

It is known that, in SOI wafers, metals that may be introduced during wafer fabrication can be gettered to the silicon/BOX interface. Subsequent thermal processing may cause the metals to migrate and degrade device yield and reliability. It can be seen from the SIMS data in figure 5.5 that, Ni and Cu are extremely fast diffusers and precipitate at the

oxide interfaces (both BOX and the 2 nm surface oxide) during the cool-down from the drive-in anneal; Fe is a much slower diffuser, and a substantial concentration of Fe may be quenched into the bulk of the wafer (as well as some surface precipitation).

The TD-SHG results from the intentionally contaminated wafers are shown in figure 5.6. It should be noted that the top native oxide layer was etched off before taking measurements. It is clear that the contaminations change the SHG responses from the wafers. For Ni, the SHG signal is significantly larger for the high contamination level, while the two lower-level measurements appear to be near or below the sensitivity limit. For Cu, the SHG response remains proportional to contamination level across the range examined, with the more pronounced difference between the two low contamination spots indicating that sensitivity may be higher for Cu. For Fe, the SHG signal does not vary significantly with contamination level. Additional experiments will be needed to better define the sensitivity and limits.

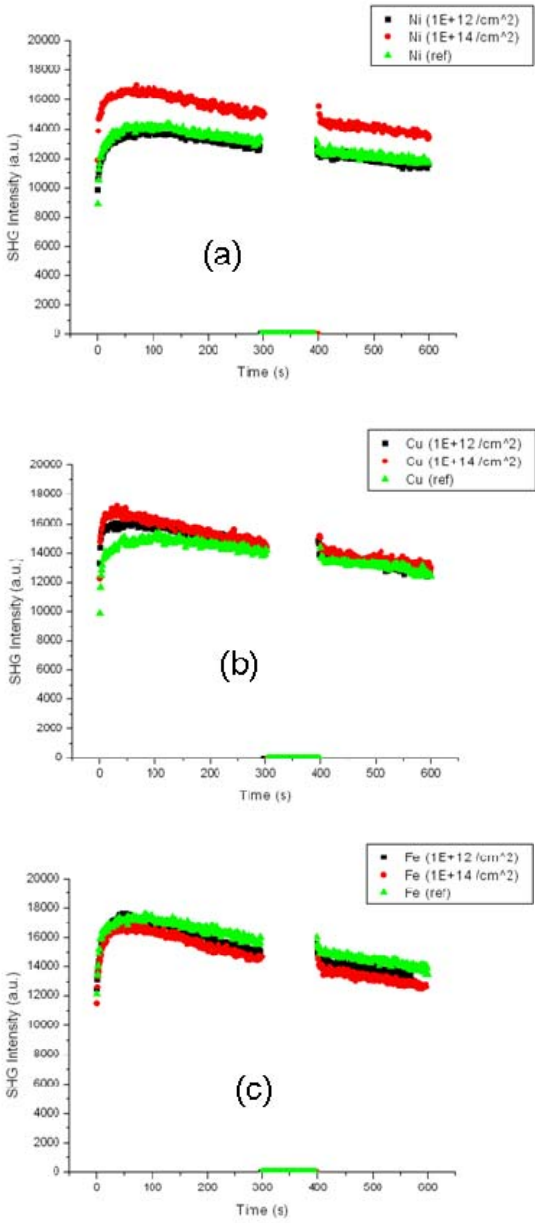

Figure 5.6. TD-SHG signals from the samples with (a) Ni contaminations, (b) Cu contaminations and (c) Fe contaminations. Noted these set of samples are after HF etching treated, which means the top native oxide layer is etched off.

We correlated the peak SHG values and μPCD lifetime maps of Ni and Cu contaminated wafers. The results are shown in figure 5.7 and figure 5.8. In the μPCD maps, the contaminated regions appear as areas of low lifetime. The SHG results show differences

that correspond to the measured differences in lifetimes. The SHG magnitude increases for higher concentrations of Ni and Cu.

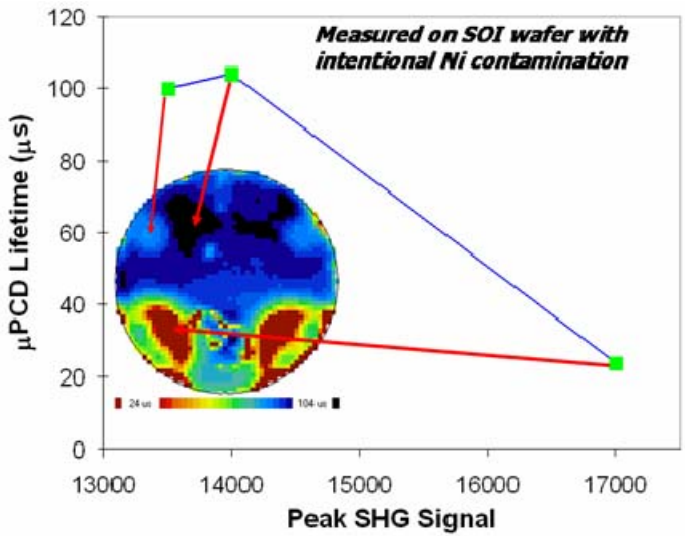

Figure 5.7. Correlation of microwave photoconductivity decay (µPCD) lifetime and peak SHG signal for intentionally Ni contaminated wafer after diffusion anneal. The inset shows the µPCD map and the arrows indicate the locations where SHG measurements were performed[74].

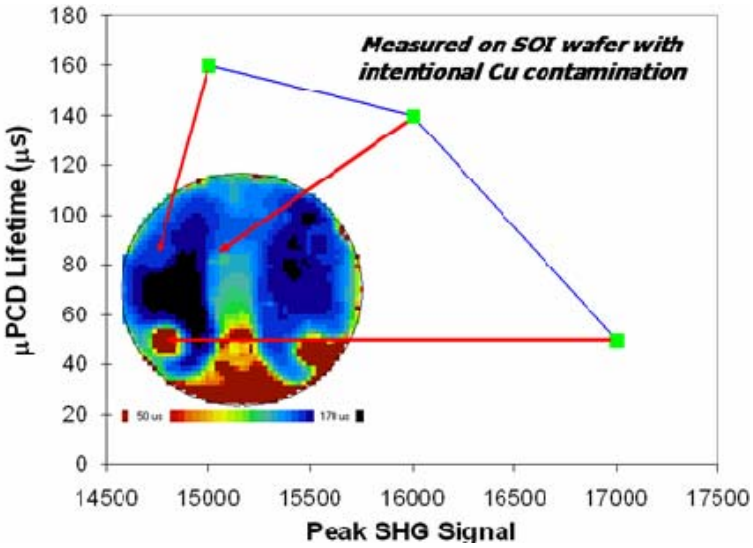

Figure 5.8. Correlation of microwave photoconductivity decay (µPCD) lifetime and peak SHG signal for intentionally Cu contaminated wafer after diffusion anneal. The inset shows the µPCD map and the arrows indicate the locations where SHG measurements were performed[74].

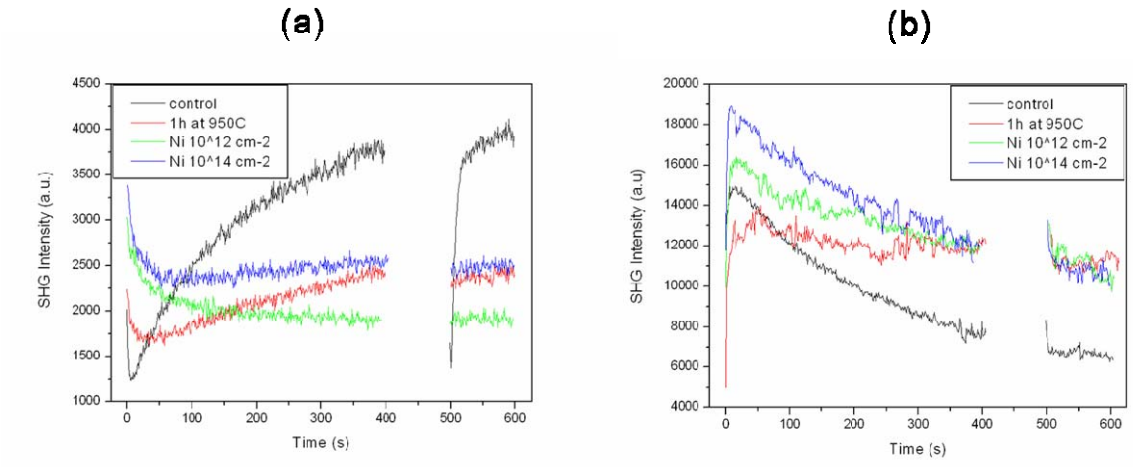

Figure 5.9. The TD-SHG measurements from Ni contaminated samples and control sample (a) with native oxide and (b) without native oxide.

Figure 5.9 shows the TD-EFISH measurement results from the control and Ni contaminated wafers with and without native oxide, respectively. The SHG signal was measured at three locations on each of the wafers before and after removal of the native oxide. Measurements were done with four different samples: the control sample has no contamination nor did it undergo any annealing processes; one sample was annealed at 950 Celsius degrees for one hour; two samples have Ni spot-contamination with two different concentrations, 10^{12} and 10^{14} cm^{-2}, respectively, and were annealed at 950 Celsius degrees for one hour. Here, it is evident that the thermal process step alone changes the response; however, the trend with contamination is much more significant. With the presence of the Ni, the change in the SHG signal goes beyond that of the uncontaminated control wafers.

5.7. SHG as a potential process control tool

In our previous studies of the SHG on SOI samples, the results have already shown that different SHG responses can be observed from wafers with different processing or characteristics[8, 71]. Here we would like to present more SHG experiments on SOI wafers and demonstrate SHG can be used as a potential process tool.

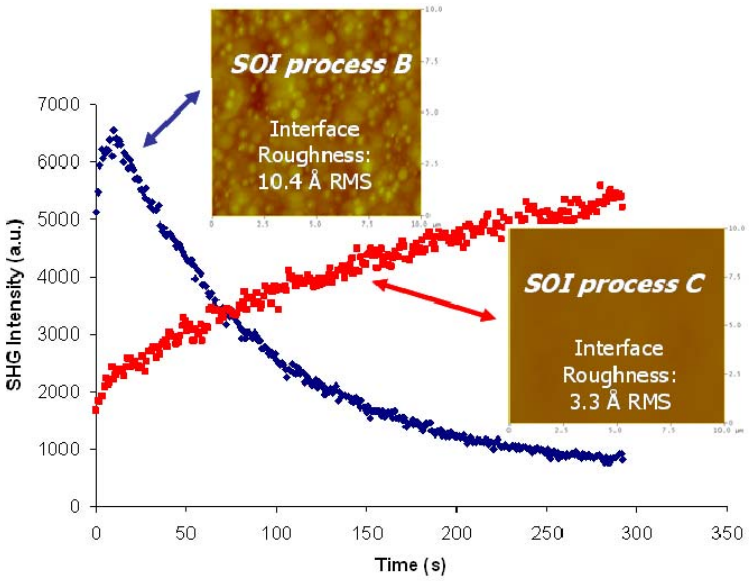

Figure 5.10. The TD-SHG signals from SIMOX SOI wafers fabricated using two different recipes. Insets show the AFM images for the top Si/BOX interface[71].

Figure 5.10 shows atomic force microscopy (AFM) images and TD-SHG responses from two SOI samples. The SOI wafers fabricated using the Separation by IMplanted OXygen (SIMOX) process were characterized by non-destructive SHG, and also by using AFM measurements of the top of the BOX following removal of the silicon device layer. Two

SIMOX process variants were measured having comparable layer thicknesses but different levels of interface roughness between the top of the BOX layer and the silicon device layer.

SHG measurements at three points across the sample produced consistent results. It can be seen from the figure that a clear difference is observed in both the peak magnitude and time dependence of the SHG signal. The interface roughness effectively increases the surface area. Also different fabrication process parameters may lead to differences in charge states at the interface. It is certain that the rougher interface is not desirable. Therefore, the difference in SHG signals provide and indication of the interface quality.

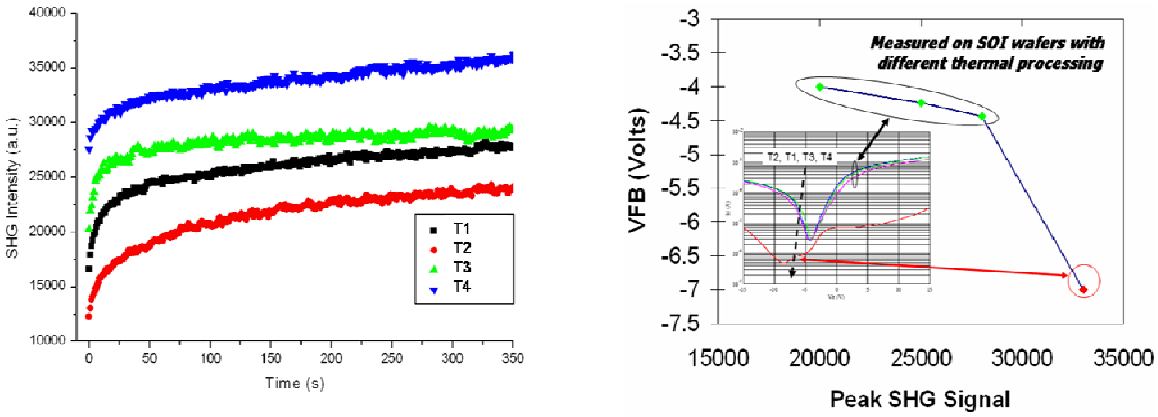

Figure 5.11. (Left) The TD-SHG data from bonded SOI wafer subjected to different thermal processes. (Right) Correlation of the TD-SHG data (a.u.) and the pseudo-MOSFET Id-Vg transfer characteristic measurements [74].

Figure 5.11 (Left) shows the TD-SHG measurements performed on four bonded SOI wafers which were subjected to different thermal processing during the fabrication. And we correlate these SHG measurements with the pseudo-MOSFET transfer characteristic measurements which is shown in figure 5.11 (Right). The thermal process appears to have limited impact over the range of temperatures from T1 to T3. However, the electrical results indicate that for temperature T4 the pseudo-MOSFET no longer shows MOSFET characteristics. This probably indicates a possible issue with the quality of the BOX or the related interfaces. From figure 5.11, it is clear that different sample properties result in different TD-SHG responses.

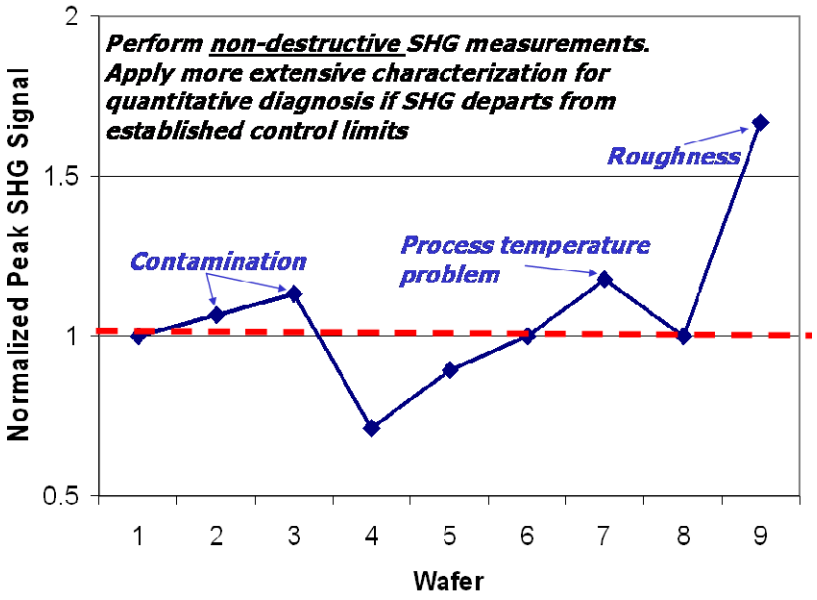

Figure 5.12. The TD-SHG experimental data normalized and combined to show schematically the potential and practical use of SHG for process control metrology[74].

The experimental results demonstrate that the SHG measurements exhibit differences that depend on SOI interface characteristics of importance to wafer manufacturers and users. Figure 5.12 illustrates schematically how SHG can be used as a method of process control metrology.

By first establishing the nominal response and control limits for the SHG signals for "good" wafers, additional quantitative destructive analysis can be limited to cases where the SHG signal extends beyond the acceptable limit(s). SHG implementation as a production monitor is compatible with commercial metrology tool configurations based on laser scanning; appropriate lasers, detectors, and wafer handling systems are available.

5.8. Conclusions

In this chapter, the second harmonic generation technique was applied to silicon-on-insulator samples and experimental data were presented. The data demonstrated that the sub-interface roughness and contamination of the SOI samples substantially change the SHG responses. We propose that the contactless and nondestructive SHG technique may provide an alternative to conventional electrical measurement techniques for characterizing buried interfaces and partially-processed wafers. Moreover, the experiment results demonstrated that application of SHG as a potential metrology tool for wafer production, which could reduce the need for sampling-based destructive testing.

CHAPTER Ⅵ

MULTI-INTERFACE SI/SIO2/MGO STRUCTURES STUDIED BY SECOND HARMONIC GENERATION

6.1. Introduction

In this chapter, we present our second harmonic generation measurements on a multi-interface $Si/SiO_2/MgO$ structure to study the effects of MgO deposition on Si/SiO2 system and charge carrier trapping and recombination in Si/SiO2 /MgO structures.

MgO, magnesium oxide, a white solid mineral, is formed by an ionic bond between one magnesium atom and one oxygen atom. It forms a cubic structure, which matches the crystal structure of salt, NaCl. Table 6.1 shows the important physical and electronic properties.

Table 6.1. Properties of MgO.

Property	**Value**	**Unit**
Crystal Structure	cubic	
Density	3.585	g/cm^3
Dielectric Constant	9.8	
Energy Gap at 300K	7.8	eV
Hardness (Mohs scale)	5.8	
Lattice Constant	4.212	$\mathring{A}$
Melting Point	~ 2800	°C
Refractive Index	1.74	
Thermal expansion at 100°C	8×10^{-6}	$°C^{-1}$

6.2. Energy band diagram

First, let's briefly recall the carrier dynamics at the interfaces in a Si/SiO_2 system.

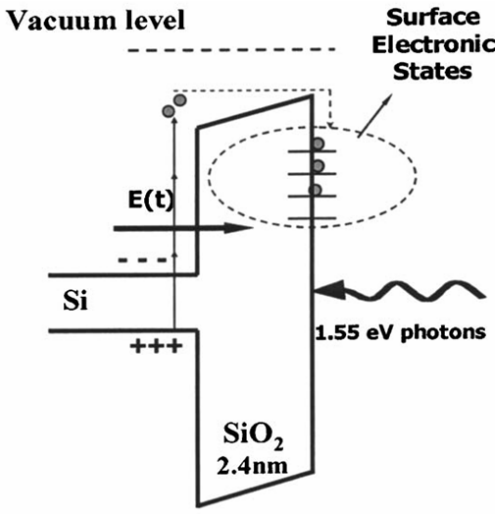

Figure 6.1. The schematic band diagram of Si/SiO_2 structure.

Electrons, excited by the photons, eject from the silicon valence band to the silicon dioxide conduction band, migrate and subsequently get trapped at the Si/SiO_2 interface and/or at the silicon dioxide surface via the ambient oxygen, as illustrated in Figure 6.1. This electron-hole separation creates an electric field across the Si/SiO_2 interface. Radiation damage can create new trap states, giving rise to higher electric field across the interface and also the trap-assisted tunneling in the system[75].

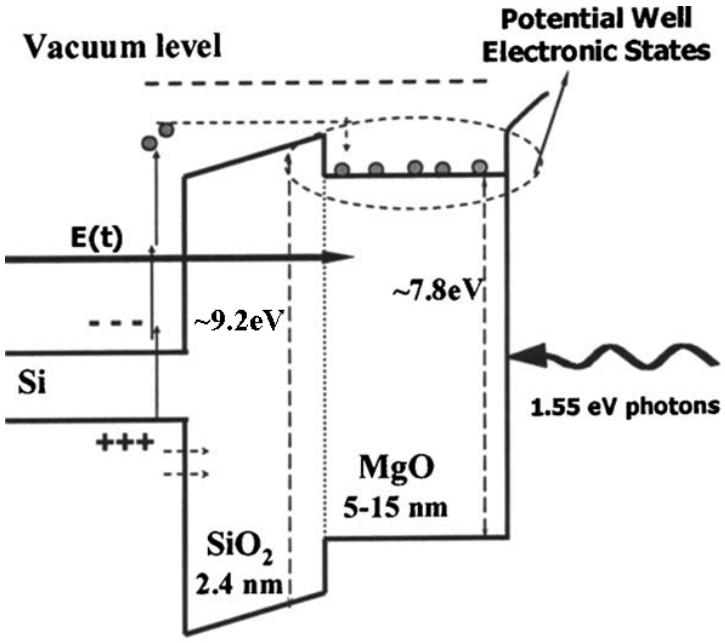

Figure 6.2. The schematic band diagram of $Si/SiO_2/MgO$ structure[76].

Different from the Si/SiO_2 system, the $Si/SiO_2/MgO$ system has an additional interface formed by SiO_2 and MgO, which subsequently changes the carrier dynamics in the system. MgO has a band gap of 7.8 eV and SiO_2 has a band gap of about 9 eV. The conduction band of MgO is at a lower energy level than the conduction band of SiO_2. We proposed that the conduction bands of these two oxides align in such a way that there is a potential well created during the deposition of MgO layer, as shown in Figure 6.2. The MgO layer and the potential well significantly change the TD-SHG response from the system. The study of the TD-SHG response can provide information of the carrier dynamics at the interfaces.

6.3. Experimental setup and procedure

There are four sets of samples were used in this experiment: first one, as a reference sample for comparison, was a 2.4 nm Si/SiO_2 sample from Lucent Technologies with thermally grown oxide film on substrate (100); the other three samples had a thin MgO layer, which has different thicknesses of 5, 10 and 15 nm, deposited on 2.4 nm Si/SiO_2 samples.

The experimental setup for the SHG measurements is illustrated in figure 4.2 in chapter 4 as a single-beam technique. A 5 W Verdi pumped Mira Ti:sapphire laser was used to irradiate on the samples. The wavelength used in these measurements was 800 nm, equivalent to photon energy of 1.5 eV. The laser pulses were directed on the sample at a 45 degree angle of incidence and focused to a spot of about 50 ~ 100 μ m. The samples were mounted on an aluminum plate, which is served as a heat sink to reduce the heating effect. The reflected fundamental and SH signals were optically separated by a prism. The SH signal was detected by a Hamamatsu photomultiplier tube (PMT) and measured by a SR 400 gated photon counter with 0.1 s temporal resolution. The iris, which was placed after the prism to block the fundamental beam, and additional blue filters, which further filtered out the fundamental beam, were applied to guarantee as least as the fundamental signal reaching the PMT detector.

Figure 6.3 is a conceptual schematic diagram of SHG from a $Si/SiO_2/MgO$ structure. The laser irradiates on the sample and a reflected second harmonic generation signal is

detected. It should be pointed out that there is SHG signal coming from both buried interfaces.

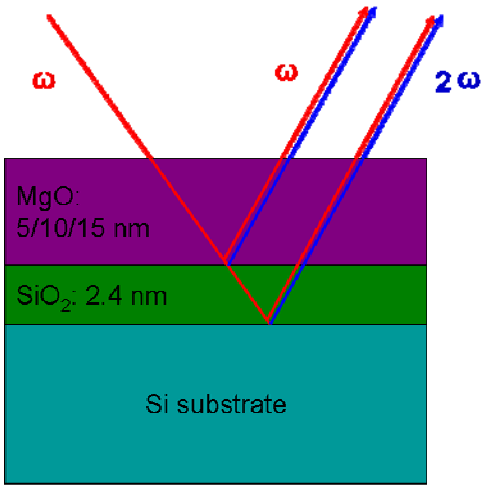

Figure 6.3. A conceptual schematic of SHG from a $Si/SiO_2/MgO$ structure.

The TD-SHG experiments were performed on these four different sets of samples at different laser power intensities. A set of neutral density filters were applied to vary the laser power intensities. The laser pulses irradiated on the sample for 360 s then were blocked for 100 s to monitor electron transport and electron-hole recombination during 'dark time' (when injection processes are interrupted). After 100 s, the laser pulses were unblocked and irradiated on the samples again.

6.4. Experimental results and discussions

Figure 6.4 shows the time dependent SHG data taken from $Si/SiO_2/MgO$ samples at high laser power, 620 mW, and low laser power, 240 mW. The small figures on the right show data from the Si/SiO_2 sample as a comparison.

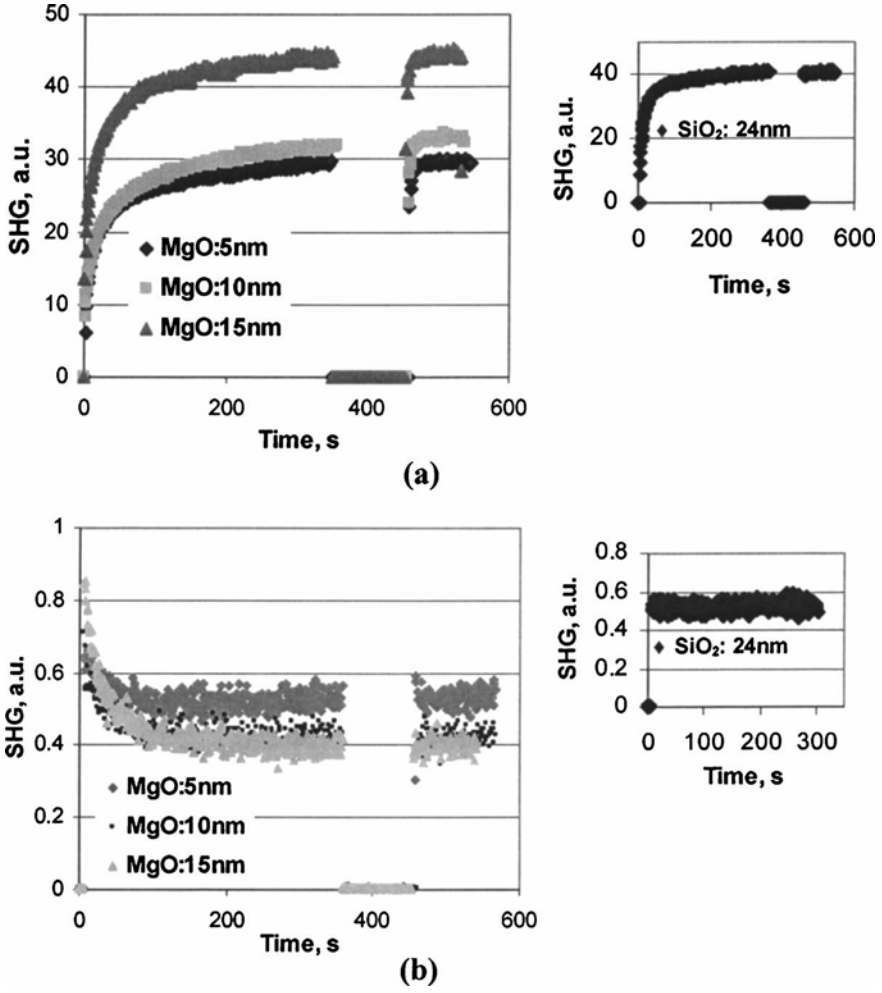

Figure 6.4. TD-SHG signals from the $Si/SiO_2/MgO$ structures at (a) high laser power of 620 mW and (b) low laser power of 240 mW. Small figures on the right are TP-SHG signals from Si/SiO_2 structure with a thickness of 2.4 nm[76].

In Figure 6.4 (a), with high laser power, after the laser pulses were unblocked, the TD-SHG signal started at a lower level than it was at the time of blocking. This indicated that there are electron-hole recombination processes present in the $Si/SiO_2/MgO$ structure. As shown in the small pictures on the right, this observation didn't show up for the Si/SiO_2 structure after the laser pulses were unblocked, which is consistent with previous work[77]. In Figure 6.4 (b), with lower laser power, the TD-SHG signal showed an initial decrease and then gradually saturated for the $Si/SiO_2/MgO$ structures. However, this pattern didn't show up in the Si/SiO_2 structure.

The decrease in the TD-SHG signal after the dark time can be due to the electron transport in the MgO potential well we proposed, as shown in Figure 6.2. Here, the band diagrams of these two different structures are listed side by side in Figure 6.5 for better understanding.

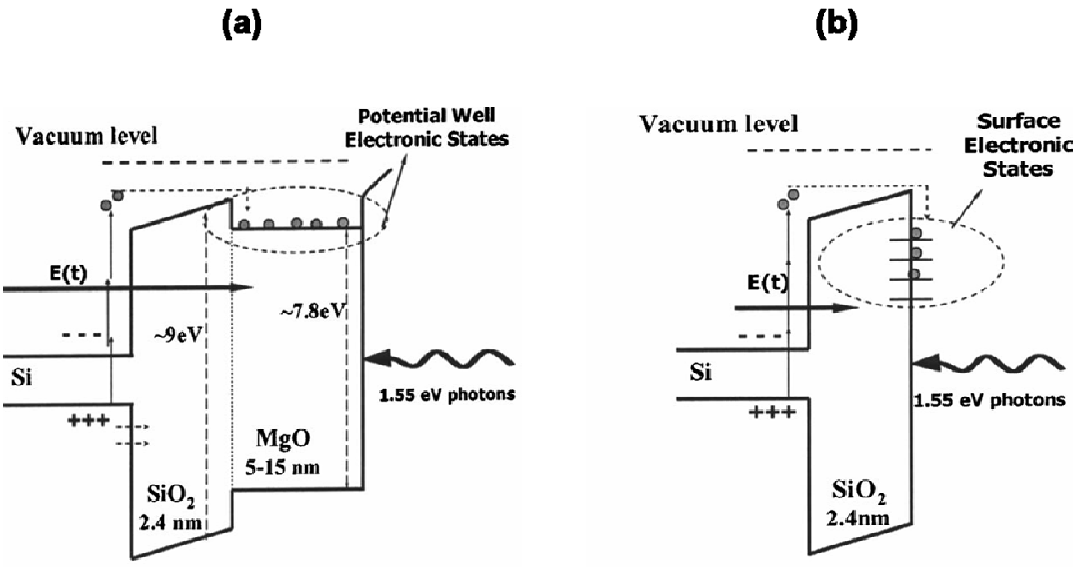

Figure 6.5. Schematic band diagrams of (a) $Si/SiO_2/MgO$ and (b) Si/SiO_2[76].

In the Si/SiO_2 structure, the electrons can only be trapped at the Si/SiO_2 interfaces or on the surface of the oxide via the ambient oxygen, as illustrated in Figure 6.5 (b). However, for the structure over-layered by MgO, electron potential-well states are available in or near the MgO conduction band. This provides a higher density of states than the structure without MgO layer. These states are at a lower energy level than the SiO_2 conduction band. This lower potential barrier makes recombination and transport processes in the oxide possible. Moreover, during the deposition of MgO layer, some defects, such as hydrogen bridge (an H atom bridging two Si atoms replacing an O atom), have been introduced into the SiO_2[78, 79]. These defects will also facilitate the trap-assisted tunneling of the electrons across the oxide and the recombination with holes. This electron-hole recombination leads to a decrease in the time-dependent SHG signal after dark time.

When the laser power is low, the SHG signal is clearly time-independent for the Si/SiO_2 structures. This is due to the fact that the electron injection from Si valence band to SiO_2 conduction is a three-photon process, which is decided by the energy barrier of about 4.3 eV and the incident laser with a photon energy of 1.55 eV. At low power, the probability of three-photon processes is very small, and electrons cannot overcome the potential barrier to be injected into the oxide.

On the other hand, for the $Si/SiO_2/MgO$ structures, the SHG signal first decreased and then gradually saturated, as shown in Figure 6.4 (b). The electron injection still cannot overcome the energy barrier. However there are new electron states in SiO_2 near the interface mostly created during the deposition of MgO layer. We attributed the decrease of SHG signal to the hole trapping in the SiO_2[80]. The 'hot' holes are created during the laser irradiation via one-/two-photon processes. These holes tunnel through the Si/SiO_2 interface and get trapped in discrete levels in the near-interfacial SiO_2, below the silicon valence band[81]. After about 100 seconds of the laser irradiation, the hole trapping saturates and so does the SHG intensity, as shown in figure 6.4(b).

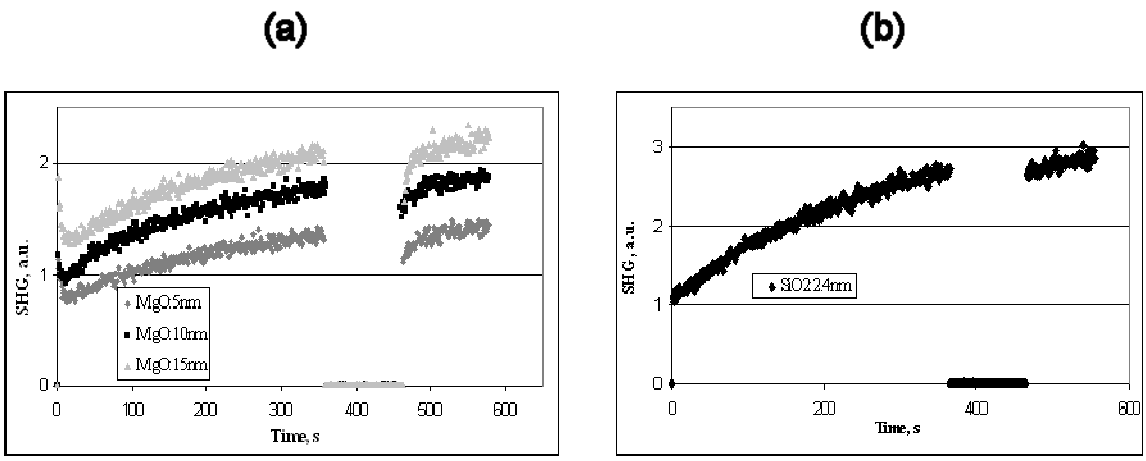

Figure 6.6. TD-SHG signal at laser power of 300 mW from (a) $Si/SiO_2/MgO$ structure and (b) Si/SiO_2 structure.

Figure 6.6 shows the TD-SHG data taken from $Si/SiO_2/MgO$ structure and Si/SiO_2 structure at the laser power of 300 mW. For the $Si/SiO_2/MgO$ structure, the SHG signal had a slight initial decrease followed by rapid increase, as seen in Figure 6.6 (a). The hole injection and trapping at the Si/SiO_2 interface in the oxide again is attributed to this observation. The electric field created due to hole injection has an opposite direction to the electric field created due to electron injection. When the electric field due to hole injection is compensated by the electric field due to electron injection, the net electric field reached minimum. After the minimum magnitude, the electron injection started to dominate and the SHG signal started to increase. Therefore, this observation is the interplay between hole injection and electron injection.

This initial decrease followed by rapid increase observation has been shown in previous work by Glinka *et al*[9, 18]. However, the observation by Glinka *et al.* may be attributed

to the interplay between an initial dipole field and the photo-induced electric field at the interface, not due to hole injection. It should be noted that hole injection process is present at any laser power. However, at high power, the electron injection process is more dominant and hole injection is overlooked.

6.5. Conclusions

The experiment has shown that the thin MgO layers deposited on Si/SiO_2 significantly changed the TD-SHG response from the material. We attributed this change to a potential well, formed by band alignment of materials in contact. The potential well created new available trapping sites with lower energy barrier, which facilitated the trap-assited tunneling across the oxide. Moreover, we observed that, at high laser power, the electron injection and trapping process dominated the carrier dynamics at the interfaces. At low laser power, the hole injection dominated and it allowed us the observe the SHG response arising from the hole injection process. This study provided new information on charge carrier dynamics in thin oxide films and showed SHG to be a very effective probe of multi-layer structures.

CHAPTER Ⅶ

TEMPERATURE DEPENDENT SECOND- AND THIRD-ORDER NONLINEAR SUSCEPTIBILITIES AT THE SI/SIO2 INTERFACE

7.1. Introduction

Electric-field induced second harmonic (EFISH) generation arising from internal photoemission has been used widely for fundamental studies of charge carrier dynamics in semiconductor/insulator systems. In this chapter, we present our work on the temperature dependent electric-field induced second harmonic generation from the Si/SiO_2 structures using the new two-color technique. The goal of this research is to understand the physical processes associated with creation of the photo-induced electric field, and extend our knowledge about effects of temperature on nonlinear optical susceptibilities at that interface. The two-color EFISH technique, used in this study, enables us to distinguish the unique contributions of each of these physical processes. Unlike single-beam experiments, the photo-induced electric field creation process in two-color experiments can be completely decoupled from the probing technique, making it an extremely sensitive tool for monitoring the transport of carriers.

We have measured the temperature dependence of the second- and third- order optical nonlinear susceptibilities, $\chi^{(2)}$ and $\chi^{(3)}$ at the Si/SiO_2 interface. A laser beam at 540 nm directed normal to the surface was used to pump electrons from the silicon valence band to trap states on the SiO_2 surface leaving the holes at or near the interface thus creating a

capacitance electric field. A second beam of wavelength 800 nm incident at 45^{o} on the same spot resulted in a second harmonic signal whose intensity was related to the varying interfacial electric field. We find that (1) the photo-induced electric field is temperature independent since the charge distributions remain unchanged after pumping, (2) both $\chi^{(2)}$ and $\chi^{(3)}$ increases as temperature increases.

7.2. Experimental configurations and procedure

The experimental setup used in the present study was similar to the one used by Marka *et al.*[42]. We used a 150 fs Ti:sapphire oscillator set to 800 nm (1.55 eV) as a probe of the second harmonic generation response. The intensity of the beam was sufficiently lowered (the peak intensity around 3.3 GW/cm^2) such that the laser beam did not contribute significantly to charge carrier injection and therefore to charge trapping. The second harmonic signal (at 400 nm) was optically separated from the fundamental beam by a prism and measured by a photomultiplier tube. Both fundamental and second harmonic beams were *p*-polarized. A tunable optical parametric generator (OPG) was used as a pump laser. The wavelength of the *s*-polarized OPG was set to 540 nm (2.3 eV), and its intensity was kept at a level that ensured creation of the electric field by internal photoemission, without significantly heating the sample. In our case, the pump laser peak intensity was about 40 GW/cm^2.

The measurements were performed on thermally grown 4.2 nm thick SiO_2 deposited on Si(100) from Lucent Technology Inc. At this oxide thickness, the photo-injected

electrons can reach the surface with a high probability, giving rise to a large, easily detectable, time-dependent EFISH signal resulting from changes in the electric field at the interface. This oxide is also thick enough that simple electron tunneling from the oxide surface back to the silicon (in the absence of assistance from defects or impurities) is negligible on the time scale of the measurements.

The sample was oriented such that the azimuthal angle of the plane of incidence was along the (110) direction. The sample was kept in a continuously flowing helium cryostat, which allowed us to perform measurements at temperatures ranging from 4.3 K to 296 K. Because the interfacial electric field sensed by EFISH in these films arises from electron trapping by ambient physisorbed oxygen at the surface of the SiO_2, its saturation level is oxygen pressure dependent. The saturation level of photo-induced electric field induced second harmonic generation decreases with decreasing pressure and vanishes around 10^{-10} Torr[47]. In our experiment the pressure in the cryostat at room temperature was kept at ~ 2 x 10^{-5} Torr to ensure that the oxygen coverage was saturated which resulted in a constant surface trap density.

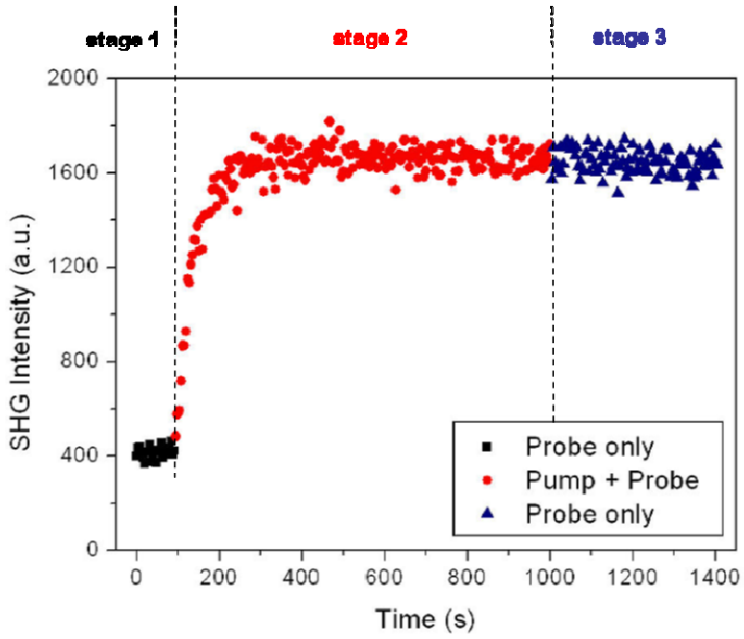

Figure 7.1. Time dependent EFISH data from Si(100)/SiO_2 with a 4.2 nm thermally grown oxide layer.

The experimental procedure was carried out in three stages, as shown in figure. 7.1. For the first about 100 seconds only the probe laser was on. That made it possible to record the SHG intensity due to the second-order optical nonlinear susceptibility without any significant charge accumulation on the SiO_2 surface. During the second stage of the experiment (900 s), both pump and probe lasers were on. The pump beam was responsible for the creation of a photo-induced electric field, arising from two-photon excitation of the electrons from the silicon valence band to the conduction band of the SiO_2, and then the transport and subsequent trapping of the electrons at the surface of the oxide. The probe laser detected the increase in the electric field at the Si/SiO_2 interface as an increase in the measured SHG intensity.

The pump photon energy of 2.3 eV makes the electron-injection from the Si valence band to the SiO_2 conduction band a two-photon process. This is determined by the fact that the band offset between Si valence band and the SiO_2 conduction band is 4.3 eV. On the other hand, the hole-injection from the Si valence band to the SiO_2 valence band is a three-photon process, a higher order process. This is determined by the fact that the band offset between Si valence band and the SiO_2 valence band is 4.7 eV. Hence, the hole-injection is much less probable than electron-injection. Also, the mobility of holes in SiO_2 is about 10^{-10} m^2 / V s, much lower than electron mobility, which is about 2 x 10^{-3} m^2 / V s[13, 14]. Therefore, most holes remain in the vicinity of the Si/SiO_2 interface. This is in contrast to the electrons that are free to move to the surface of the SiO_2 and be trapped by the ambient oxygen.

During the third and last stage of the experiment, the pump laser was off again, while the probe laser was able to monitor the electric field arising from the trapped electrons and holes. In our case, no significant back-tunneling of the electrons through the oxide was observed at any of the temperatures, indicating a relatively low density of defects and impurities with energy levels within the SiO_2 band gap.

It has been reported that heating effects due to the femtosecond laser pulses can affect the SHG response in some cases[30]. One can easily estimate if this affects the measurements presented here. We first consider possible heating due to the pump laser. As can be seen in Fig. 1, after the pump beam is blocked, the EFISH saturation intensity remains at the same level. This is an indication that, not only is electron tunneling from

the oxide surface back to the silicon negligible, but also that heating effects are negligible. A similar test was performed with the probe laser. Blocking and unblocking the probe beam showed no variation in SHG response due to possible heating/cooling of the sample.

7.3. Experimental results and discussions

7.3.1. Temperature dependence of second-order nonlinear susceptibility

The time dependent EFISH signals from Si/SiO_2 at four different temperatures are shown in figure 7.2. It is clear that SHG intensities, both initial and saturation values, increase with temperature. A previous study of temperature dependence of linear susceptibility $\chi^{(1)}$ indicates that the reflectivity differs by less than 3% in the temperature range between 10K and 300K[82]. This small difference is negligible compared to the difference of SHG intensities, which is greater than 40%. Thus, in this paper, we attribute changes in SHG intensities solely to temperature variations in the nonlinear susceptibilities.

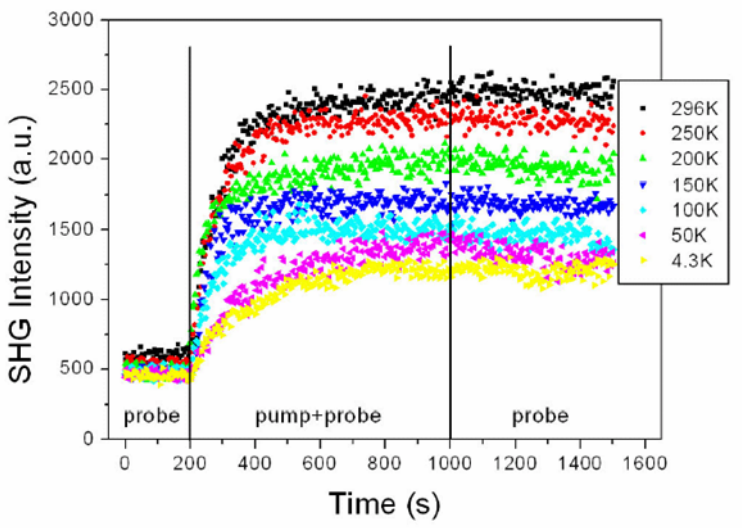

Figure 7.2. TD-EFISH measurements from a Si(100)/SiO_2 (4.2 nm) interface as a function of temperature[83].

The intensity of the electric field induced second harmonic generation can be described by

$$I^{(2\omega)}(t) = \left|\chi^{(2)} + \chi^{(3)}E(t)\right|^2 \left(I^{(\omega)}\right)^2, \tag{7.1}$$

where $I^{(\omega)}$ and $I^{(2\omega)}(t)$ are the intensities of the fundamental and the time-dependent SHG beams, respectively. Here $\chi^{(2)}$ is the second-order susceptibility, $E(t)$ is a photo-induced electric-field present at the interface, and $\chi^{(3)}$ is the third-order nonlinear susceptibility.

It should be pointed out that the probe laser is set at wavelength of 800 nm with a photon energy of 1.5 eV in our experiment. Si is an indirect band gap semiconductor and the interband absorption spectrum shows that the absorption coefficient is very low at 1.5

eV[84]. Also, SiO_2 has a band gap of 9 eV and it is transparent to a laser with photon energy of 1.5 eV. Therefore, Si and SiO_2 are lossless medium in this set up and both $\chi^{(2)}$, $\chi^{(3)}$ are real numbers[85].

For centrosymmetric systems, such as crystalline silicon, second-order nonlinear optical susceptibility vanishes under the dipole approximation, but at the interface the symmetry is broken and second-order nonlinear processes are allowed. The contribution from nonlocal quadrupole bulk contribution is allowed. However, the bulk oxide third-order susceptibility is about 10^4 smaller than for bulk Si[44]. Also, there is no electric field present in the bulk Si other than the optical field. Thus, both $\chi^{(2)}$, $\chi^{(3)}$ represent only the Si/SiO_2 interface.

Since the initial EFISH intensity can be described as

$$I^{(2\omega)} = \left|\chi^{(2)}\right|^2 (I^{(\omega)})^2 \tag{7.2}$$

by analysis of the initial EFISH values, we obtained the temperature dependence of the effective second-order susceptibility, which is shown in figure 7.3. This observation is consistent with previous results obtained by Suzuki *et al*[86] and Dadap *et al*[29] for higher temperatures. A broad peak of two-photon E_1 resonance in the silicon second harmonic spectrum red-shifts and broadens with increasing temperature. This thermally enhanced SHG due to the second-order susceptibility contribution is a combination of (1)

the thermal expansion of the lattice coupled with the change of the electron energies with volume and renormalization of band energies by electron-phonon interaction[87, 88], and (2) the difference between the thermal expansion coefficients of silicon and SiO_2, which can strain the interface between those two materials, and change the observed SHG response[35].

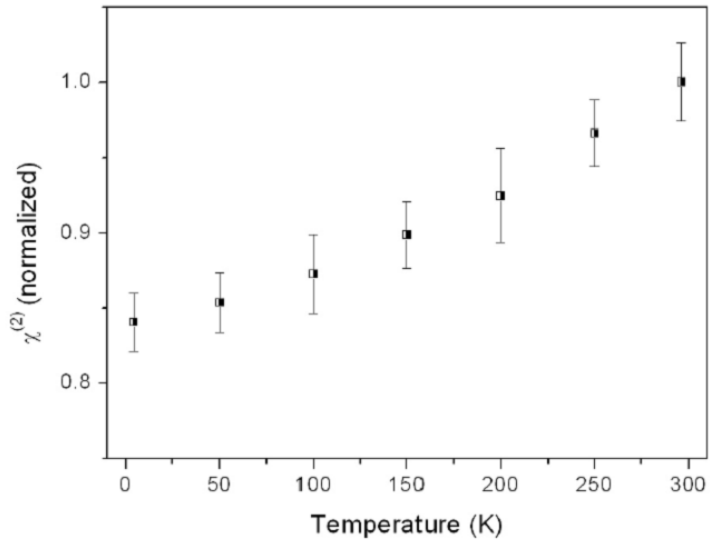

Figure 7.3. Temperature dependence of the second-order nonlinear susceptibility[83].

7.3.2. Temperature independent photo-induced electric field

The electric field in equation (7.1) arises from charge separation due to multi-photon excitation of electrons in the valence band of silicon above the conduction band of SiO_2, the subsequent transport of these electrons across the oxide, and trapping at the surface of the oxide by ambient oxygen[47, 48]. Van Driel and co-authors suggest that ambient

oxygen captures the electrons at the surface of the SiO_2 because of the high electron affinity of the oxygen. The electrons and oxygen attract each other in a harpooning reaction in the vicinity of the SiO_2/ambient interface and then attach to or even penetrate the positively charged solid[89]. It also has been shown that the saturation EFISH intensity varies with the oxygen pressure because of the change in the number of available electronic trap states for photo-injected electrons. The combined measurements of photoemission currents and the contact-potential-difference confirm that photo-induced gas-assisted charging gives rise to the second harmonic generation induced by internal photoemission in thin Si/SiO_2 films[51]. For a 1.6 nm oxide the maximum near-interface electric field in the oxide was estimated to be ~0.6 MV/cm, giving a surface charge density of 5×10^{11} cm^{-2} (assuming an oxide dielectric constant of ~ 3.8).

The value of EFISH saturation intensity is determined not only by the electric field present at the interface, but also by the second and third-order optical nonlinear susceptibilities as shown in equation (7.1). Photo-induced electric fields are a measure of the surface electron density:

$$E(t) = \sigma(t)/\varepsilon_{Si} \,, \tag{7.3}$$

where the surface electron density $\sigma(t)$ is proportional to the number of filled electronic trap states at the surface of the oxide. This photo-induced electric field at the Si/SiO_2 interface is proportional to the number of filled electronic trap states, and can be

expressed by a rate equation[42, 43]. In the case of the system where only electron dynamics contribute to the electric field, this can be written as:

$$\frac{dn_e}{dt} = \frac{(n_{0e} - n_e)}{\tau^{e}_{trapping}} - \frac{n_e}{\tau^{e}_{detrapping}}, \tag{7.4}$$

where n_{0e} is the initial number of the unfilled electronic trap states, and $1/\tau^{e}_{trapping}$ is the trapping rate of states due to electron injection caused by the pump laser beam (as mentioned above, electron injection due to the probe laser can be neglected). The value of $1/\tau^{e}_{detrapping}$ is related to the lifetime of surface electronic trap states. The last term in equation (7.4) can be neglected because, for the 4.2 nm thick SiO_2, the value of $\tau^{e}_{detrapping}$ is significantly greater than $\tau^{e}_{trapping}$. In that case, the number of filled electronic surface trap states can be described by the simplified expression

$$n_e(t) = n_{0e}\left(1 - \exp\left[-t/\tau^{e}_{trapping}\right]\right). \tag{7.5}$$

By introducing equation (7.5) into (7.1), it can be shown that the difference between the initial and saturation intensities of photo-induced EFISH is a function of the second and third-order optical nonlinear susceptibilities and the number of available electronic trap states:

$$\Delta I^{(2\omega)} = I^{(2\omega)}(\infty) - I^{(2\omega)}(0) = \left((\chi^{(3)} n_{0e})^2 + 2\chi^{(2)}\chi^{(3)} n_{0e}\right)(I^{\omega})^2. \tag{7.6}$$

Our data clearly show that $\chi^{(2)}$ changes with temperature. To explain the differences in the EFISH saturation intensity values, the temperature dependences of the third-order optical nonlinear susceptibility $\chi^{(3)}$ and number of filled electronic trap states must be investigated.

The two-color EFISH technique allows us to saturate surface electronic trap states at a given temperature by the pump laser. Once the saturation of the EFISH is reached, the pump laser can be blocked, and we can directly follow the change in saturation intensity as a function of temperature using the probe laser only. This ensures that no additional electric field is created when the temperature is changed.

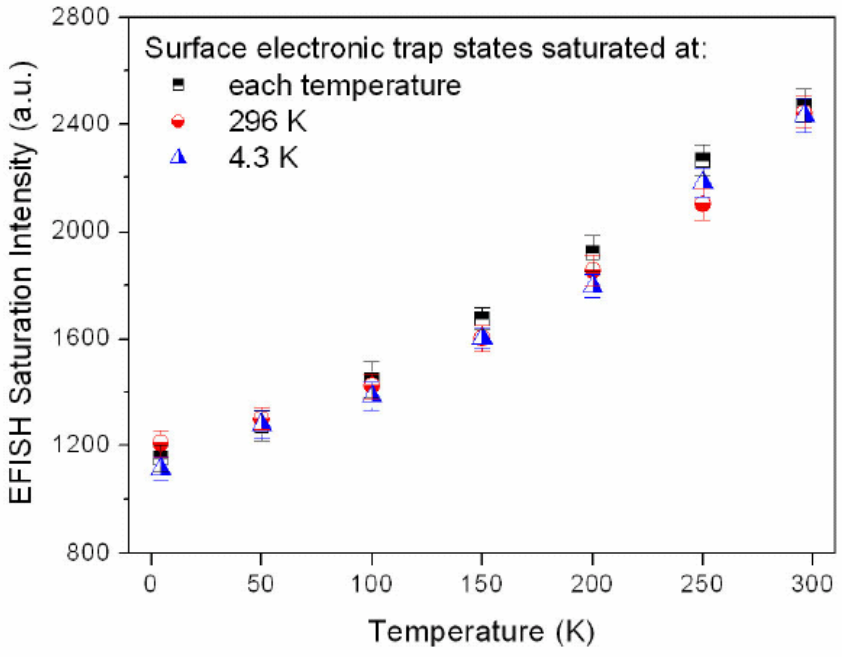

Figure 7.4. Temperature dependence of EFISH saturation intensities[83].

Figure 7.4 shows values of EFISH saturation intensities as a function of temperature. First, the EFISH saturation was obtained at 296 K, and pump laser was turned off (Figure 7.4, circles). Then the temperature was gradually decreased down to 4.3 K while the second harmonic intensity was monitored by the probe laser. A similar measurement was performed for the saturation obtained at 4.3 K, followed by increasing temperature (Figure 7.4, triangles). Those results were compared to the values obtained when surface electronic trap states were filled by the pump laser at each temperature independently (Figure 7.4, squares). All of these values are comparable to the experimental error. *We conclude that the photo-induced electric field, which is related to the number of filled surface electronic trap states, is independent of temperature.* This shows that the increase in EFISH saturation intensity, as shown in figure 7.2, is due entirely to the temperature dependent variations in $\chi^{(2)}$ and $\chi^{(3)}$, and not due to changes in the value of the photo-induced electric field.

7.3.3. Temperature dependence of third-order nonlinear susceptibility

Since the temperature dependence of the second-order nonlinear susceptibility has been determined in our experiments, and the number of filled electronic trap states and thereby the electric field was shown to be constant, it is possible to find the temperature dependence of the third-order nonlinear susceptibility using equation (7.6). The third-order nonlinear susceptibility was found to exhibit a nearly linear behavior, as shown in figure 7.5. One can represent the observed SHG intensities as far-field radiation from dipoles driven in a non-harmonic fashion by the incident electric field[90]. The photo-

induced electric field created at the interface will change this potential, giving rise to an additional SH signal. The third-order nonlinear susceptibility represents the coupling between the electric field produced by the incident light and the photo-induced electric field present at the interface. Since $\chi^{(3)}$ is related to the polarization in a similar manner as the $\chi^{(2)}$, similar reasons may account for its thermal dependence. However, the detailed explanation of its behavior is a fruitful topic for future work.

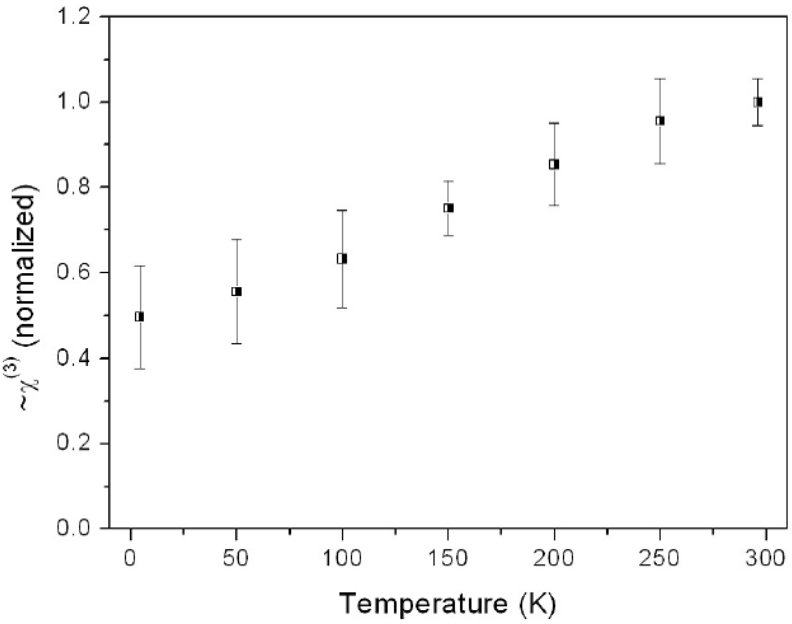

Figure 7.5. Temperature dependence of third-order nonlinear susceptibility[83].

7.3.4. Temperature dependence of the trapping rate $\frac{1}{\tau^{e}_{trapping}}$

Here we focus on analyzing the EFISH data taken with both pump and probe lasers in operation as shown in figure 7.2 (stage 2), resulting from the pump laser excitation. From these measurements, we can obtain the trapping rate $\frac{1}{\tau^{e}_{trapping}}$ as a function of temperature.

For each temperature, we fitted the time dependent EFISH data to the formula,

$$I^{(2\omega)}(t) = | a_0 + b \cdot (1 - e^{-t/\tau^{e}_{trapping}}) |^2, \tag{7.7}$$

where a_0 and b are phenomenological values, related to the initial and saturation EFISH intensities in order to determine $\tau^{e}_{trapping}$. Having acquired $\tau^{e}_{trapping}$, we determined the trapping rate $\frac{1}{\tau^{e}_{trapping}}$ for each temperature and plotted it in figure 7.6. Note that the trapping rate appears to peak at around 120 K and is nonsymmetric.

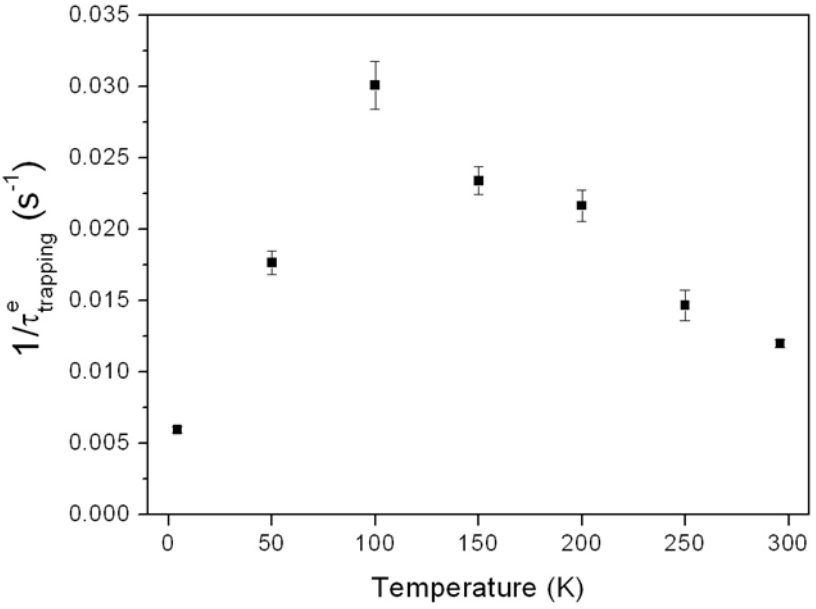

Figure 7.6. Temperature dependence of the trapping rate $\frac{1}{\tau^{e}_{trapping}}$ for Si/SiO_2.[83]

It should be pointed out that our previous analysis of the pump power dependent measurements have shown that, at a pump photon energy of 2.3 eV, electron excitation from the silicon valence band to above the conduction band of SiO_2 is a two-photon process at all temperatures. This is an indication that, although the band gap of the Si increases at low temperatures, the band offset at the Si/SiO_2 interface remains less than 4.6 eV.

At higher temperatures above about 120 K, electron-phonon scattering reduces the transport rate as a function of increasing temperature[91]. This is because the density of phonons in solids increases with temperature. The scattering time due to this mechanism will decrease with temperature as will the transport rate across the oxide.

Now, let us consider the possible effects causing the increase of trapping rate $\frac{1}{\tau^{e}_{trapping}}$ at low temperature (below ~120 K). We attribute this observation to a combination of two effects. First, the absorption coefficient of Si increases as temperature increases[13], which directly leads to the increase of photon absorption rate. Even though electron-injection is a two-photon process at all temperatures, the higher photon absorption rate makes the photon absorption easier and results in a higher electron-hole pair production rate. Second, the photo-induced electric field E_0 due to electron-hole pair separation polarizes the SiO_2. The resulting electric field E_p due to the polarization decreases the effective electric field in the bulk SiO_2. The effective electric field affects the transport of electrons in SiO_2 and consequently affects the trapping rate of electrons. E_0 and E_p are related by χ according to

$$E_p = -\chi^{(1)} E_0 . \tag{7.8}$$

Here, the minus sign denotes the opposite directions of E_0 and E_p. $\chi^{(1)}$ is the linear susceptibility of SiO_2 and is related to dielectric constant ε, and refractive index n.

$$\begin{aligned} n &= \sqrt{\varepsilon} \\ \varepsilon &= \varepsilon_0 (1+\chi) \end{aligned} . \tag{7.9}$$

ε_0 is the electric permittivity of free space. Previous study of temperature dependence of the SiO_2 refractive index n showed that n increases with increasing temperature[92].

From (7.9), it is clear that $\chi^{(1)}$ also increases as temperature increases. Because we already concluded that photo-induced electric field E_0 is temperature independent, E_p increases as temperature increases according to equation (7.8). This temperature dependence of E_p consequently decreases the effective electric field in bulk SiO_2 as temperature increases. This reduced effective electric field in bulk SiO_2 assists the flux of electrons transport through the oxide. These two effects together result in the observation that $\frac{1}{\tau^{e}_{trapping}}$ increases with increasing temperature at low temperature. The non-symmetric behavior of $\frac{1}{\tau^{e}_{trapping}}$ at low and high temperatures is a competition result of these two effects and the electron-phonon scattering.

7.4. Conclusions

In this chapter, temperature dependent SHG experiment on Si/SiO_2 samples was carried out. From this experiment, we had four important results.

First, the initial SHG intensities data at stage one showed that second-order susceptibility increases with increasing temperature. Second, by studying the SHG saturation levels at stage three, we concluded that the number of filled electron trap states at the oxide surface, which is directly related to the photo-induced electric field, did not change with temperature. Third, by analyzing the SHG saturation levels at stage three, we deduced that the third-order nonlinear optical susceptibility also increased with temperature. Fourth, from the time dependent EFISH data at stage two, we obtained the trapping rate

as a function of temperature. It peaked around 120 K with nonsymmetric behavior. Its behavior is caused by the combination effect of electron-phonon scattering, temperature dependence of the Si absorption coefficient and the SiO_2 dielectric constant.

CHAPTER Ⅶ

SUMMARY

In this thesis, we review the theoretical background of second harmonic generation (SHG) and electric field induced second harmonic generation (EFISH). We also review previous researches associated EFISH measurements from various groups. Then, we report our SHG experiments to study the buried interfaces in different material structures. SHG has shown to be a noninvasive, contactless and unique technique sensitive to interface roughness, defects and contamination.

Our recent SHG studies of silicon-on-Insulator showed that the SHG measurements exhibit differences that depend on SOI interface roughness and contamination, which are of importance to wafer manufacturers and users. The experimental results presented here demonstrated that the application of SHG can be a promising alternative for the conventional destructive electrical measurement to characterize the interface properties and detection of sub-surface contamination in SOI wafers.

Our measurements of $Si/SiO_2/MgO$ structures by SHG showed that the deposited MgO layer significantly changed the SHG responses from the system. We proposed that a potential well is formed by band alignment of MgO and SiO_2, which facilitates the trap-assisted tunneling across the oxide. It is shown that at low laser intensity, hole injection into the interfacial SiO_2 appears to dominate the trapping response. At high laser power,

the three-photon processes lead to electron injection that first saturates the trapped holes, and then leads to excess electron trapping. It is clear that SHG offers significant advantages for studying charge carrier dynamics in thin oxides and multi-interface structures.

Our work on temperature dependence of electric field induced second harmonic generation in Si/SiO_2 experiment helped us better understand the physical processes associated with creation of the photo-induced electric field. The experimental data show that the second- and third-order nonlinear susceptibilities increased with temperature. The data also show that the number of filled electron trap states at the oxide surface, which is related to the photo-induced electric field, doesn't change with temperature. Moreover, the temperature dependence of the trapping rate is a combination effect of electron-phonon scattering, temperature dependence of the Si absorption coefficient and the SiO_2 dielectric constant.

In summary, we demonstrated that second harmonic generation is an effective, noninvasive, nondestructive technique for characterization of thin oxide and multi-interface structures.

REFERENCES

1. Franken, P.A., et al., *Generation of Optical Harmonics.* Physical Review Letters, 1961. **7**(4): p. 118.

2. Maiman, T.H., *Stimulated Optical Radiation in Ruby.* Nature, 1960. **187**: p. 493-494.

3. Bloembergen, N. and P.S. Pershan, *Light Waves at the Boundary of Nonlinear Media.* Physical Review, 1962. **128**(2): p. 606.

4. Ducuing, J. and N. Bloembergen, *Observation of Reflected Light Harmonics at the Boundary of Piezoelectric Crystals.* Physical Review Letters, 1963. **10**(11): p. 474.

5. Bloembergen, N. and J. Ducuing, *Experimental verification of optical laws of non-linear reflection.* Physics Letters, 1963. **6**(1): p. 5-6.

6. Chang, R.K., J. Ducuing, and N. Bloembergen, *Relative Phase Measurement Between Fundamental and Second-Harmonic Light.* Physical Review Letters, 1965. **15**(1): p. 6.

7. Abdullaev, A.Y., et al., *Nonlinear Optical Diagnostics of Thermal-Oxidation Tion-Induced Silicon Lattice Deformation.* Fizika Tverdogo Tela, 1987. **29**(6): p. 1898-1901.

8. Jun, B., et al., *Charge trapping in irradiated SOI wafers measured by second harmonic generation.* Ieee Transactions on Nuclear Science, 2004. **51**(6): p. 3231-3237.

9. Glinka, Y.D., et al., *Characterization of charge-carrier dynamics in thin oxide layers on silicon by second harmonic generation.* Physical Review B, 2002. **65**(19): p. 193103.

10. Education, T.J.N.A.F.-O.o.S. *It's Elemental*. 2008 [cited; Available from: http://education.jlab.org/itselemental/ele014.html.

11. Laboratory, L.A.N. 2008 [cited; Available from: http://periodic.lanl.gov/elements/14.html.

12. ASA, R.E.C., *Analyst Silicon Field Trip*. 2007.

13. Sze, S.M., *Physics of Semiconductor Devices*. 2nd ed. 1981, New York: Wiley-Interscience. 880.

14. McGuire, G.E., *Semiconductor Materials and Process Technology Handbook*. 1988, Park Ridge, New Jersey: Noyes Publications. 675.

15. Hughes, R.C., *Hole mobility and transport in thin SiO2 films.* Applied Physics Letters, 1975. **26**(8): p. 436.

16. Helms, C.R., *the Si-SiO2 System* 1988: Elsevier.

17. Hughes, R.C., *Charge-Carrier Transport Phenomena in Amorphous SiO2: Direct Measurement of the Drift Mobility and Lifetime.* Physical Review Letters, 1973. **30**(26): p. 1333.

18. Balk, P., *the Si-SiO2 System*. 1988: Elsevier.

19. Wang, W., et al., *Coupled electron-hole dynamics at the Si/SiO2 interface.* Physical Review Letters, 1998. **81**(19): p. 4224-4227.

20. Shen, Y.R., *the Principles of Nonlinear Optics*. 1984, New York: John Wiley.

21. Boyd, R.W., *Nonlinear Optics*. 1992, Boston: Academic Press.

22. Dempsey R.J., D.D.G., Buice R.G. Jr., Lodder R.A. *Driven to depth: biological and medical applications of near-infrared spectrometry*. 2008 [cited 2008; Available from: http://www.pharm.uky.edu/ASRG/Papers/Depth/depth.html.

23. Heinz, T.F., M.M.T. Loy, and W.A. Thompson, *Study of Si(111) Surfaces by Optical 2nd-Harmonic Generation - Reconstruction and Surface Phase-Transformation.* Physical Review Letters, 1985. **54**(1): p. 63-66.

24. Cundiff, S.T., et al. *Second-harmonic generation at the interface between Si(100) and thin SiO[sub 2] layers*. in *Papers from the 44th national symposium of the AVS*. 1998. San Jose, California (USA): AVS.

25. Cundiff, S.T., et al., *Si/SiO[sub 2] interface roughness: Comparison between surface second harmonic generation and x-ray scattering.* Applied Physics Letters, 1997. **70**(11): p. 1414-1416.

26. Bjorkman, C.H., et al., *Influence of Surface-Roughness on the Electrical-Properties of Si-Sio2 Interfaces and on 2nd-Harmonic Generation at These Interfaces.* Journal of Vacuum Science & Technology B, 1993. **11**(4): p. 1521-1527.

27. Dadap, J.I., et al., *Randomly Oriented Angstrom-Scale Microroughness at the Si(100) Sio2 Interface Probed by Optical 2nd-Harmonic Generation.* Applied Physics Letters, 1994. **64**(16): p. 2139-2141.

28. Fomenko, V., E.P. Gusev, and E. Borguet, *Optical second harmonic generation studies of ultrathin high-k dielectric stacks.* Journal of Applied Physics, 2005. **97**(8).

29. Dadap, J.I., et al., *Second-harmonic spectroscopy of a Si(001) surface during calibrated variations in temperature and hydrogen coverage.* Physical Review B, 1997. **56**(20): p. 13367-13379.

30. Dadap, J.I., et al., *Analysis of second-harmonic generation by unamplified, high-repetition-rate, ultrashort laser pulses at Si(001) interfaces.* Ieee Journal of Selected Topics in Quantum Electronics, 1995. **1**(4): p. 1145-1155.

31. Hofer, U., L.P. Li, and T.F. Heinz, *Desorption of Hydrogen from Si(100)2x1 at Low Coverages - the Influence of Pi-Bonded Dimers on the Kinetics.* Physical Review B, 1992. **45**(16): p. 9485-9488.

32. Hu, X.F., et al., *In situ optical second-harmonic-generation monitoring of disilane adsorption and hydrogen desorption during epitaxial growth on Si(001).* Applied Physics Letters, 1997. **71**(10): p. 1376-1378.

33. Xu, Z., et al., *Second harmonic spectroscopy of Si(001) surfaces: Sensitivity to surface hydrogen and doping, and applications to kinetic measurements.* Journal of Vacuum Science & Technology B, 1997. **15**(4): p. 1059-1064.

34. Bratu, P. and U. Hofer, *Phonon-Assisted Sticking of Molecular-Hydrogen on Si(111)-(7x7).* Physical Review Letters, 1995. **74**(9): p. 1625-1628.

35. Govorkov, S.V., et al., *Laser Nonlinear-Optical Probing of Silicon/Sio2 Interfaces - Surface Stress Formation and Relaxation.* Applied Physics a-Materials Science & Processing, 1990. **50**(4): p. 439-443.

36. Daum, W., et al., *Identification of Strained Silicon Layers at Si-Sio2 Interfaces and Clean Si Surfaces by Nonlinear-Optical Spectroscopy.* Physical Review Letters, 1993. **71**(8): p. 1234-1237.

37. Alexandrova, S., P. Danesh, and I.A. Maslyanitsyn, *Second harmonic generation in hydrogenated amorphous silicon.* Physical Review B, 2000. **61**(16): p. 11136.

38. Miyashita, Y., et al., *Effect of Stress on Second Harmonic Generation in TeO2-based Glass Ceramics.* Journal of the Ceramic Society of Japan, 2004. **112**: p. S1257-S1261.

39. Ito, F. and H. Hirayama, *2nd-Harmonic Generation from Sio2/Si(111) Interfaces.* Physical Review B, 1994. **50**(15): p. 11208-11211.

40. Sipe, J.E., D.J. Moss, and H.M. Vandriel, *Phenomenological Theory of Optical 2nd-Harmonic and 3rd-Harmonic Generation from Cubic Centrosymmetric Crystals.* Physical Review B, 1987. **35**(3): p. 1129-1141.

41. Hollering, R.W.J., *Angular-Dependence of Optical 2nd-Harmonic Generation at a Ge(111) Surface.* Journal of the Optical Society of America B-Optical Physics, 1991. **8**(2): p. 374-377.

42. Marka, Z., et al., *Two-color optical technique for characterization of x-ray radiation-enhanced electron transport in SiO2.* Journal of Applied Physics, 2003. **93**(4): p. 1865-1870.

43. Marka, Z., et al., *Band offsets measured by internal photoemission-induced second-harmonic generation.* Physical Review B, 2003. **67**(4).

44. Mihaychuk, J.G., N. Shamir, and H.M. van Driel, *Multiphoton photoemission and electric-field-induced optical second-harmonic generation as probes of charge transfer across the Si/SiO2 interface.* Physical Review B, 1999. **59**(3): p. 2164-2173.

45. Aktsipetrov, O.A., et al., *dc-electric-field-induced and low-frequency electromodulation second-harmonic generation spectroscopy of Si(001)-SiO2 interfaces.* Physical Review B, 1999. **60**(12): p. 8924-8938.

46. E.H. Poindexter, E.R.A., P.J. Coplan, *The physics of SiO2 and its interfaces*, ed. S.T. Pantelides. 1978, New York: Pergamon. 227.

47. Bloch, J., J.G. Mihaychuk, and H.M. vanDriel, *Electron photoinjection from silicon to ultrathin SiO2 films via ambient oxygen.* Physical Review Letters, 1996. **77**(5): p. 920-923.

48. Mihaychuk, J.G., et al., *Time-Dependent 2nd-Harmonic Generation from the Si-Sio2 Interface Induced by Charge-Transfer.* Optics Letters, 1995. **20**(20): p. 2063-2065.

49. Shamir, N., J.G. Mihaychuk, and H.M. van Driel, *Trapping and detrapping of electrons photoinjected from silicon to ultrathin SiO2 overlayers. I. In vacuum and in the presence of ambient oxygen.* Journal of Applied Physics, 2000. **88**(2): p. 896-908.

50. Shamir, N., J.G. Mihaychuk, and H.M. vanDriel, *Transient charging and slow trapping in ultrathin SiO2 films on Si during electron bombardment.* Journal of Vacuum Science & Technology a-Vacuum Surfaces and Films, 1997. **15**(4): p. 2081-2084.

51. Shamir, N. and H.M. van Driel, *Trapping and detrapping of electrons photoinjected from silicon to ultrathin SiO2 overlayers. II. In He, Ar, H-2, N-2, CO, and N2O.* Journal of Applied Physics, 2000. **88**(2): p. 909-917.

52. Shamir, N., et al., *Universal mechanism for gas adsorption and electron trapping on oxidized silicon.* Physical Review Letters, 1999. **82**(2): p. 359-361.

53. Berglund, C.N. and R.J. Powell, *Photoinjection into Sio2 - Electron Scattering in Image Force Potential Well.* Journal of Applied Physics, 1971. **42**(2): p. 573-&.

54. McGilp, J.F., *A review of optical second-harmonic and sum-frequency generation at surfaces and interfaces.* Journal of Physics D-Applied Physics, 1996. **29**(7): p. 1812-1821.

55. Adamchuk, V.K. and V.V. Afanas'ev, *Internal photoemission spectroscopy of semiconductor-insulator interfaces.* Progress in Surface Science, 1992. **41**(2): p. 111-211.

56. Robertson, J. *Band offsets of wide-band-gap oxides and implications for future electronic devices*. in *Papers from the international conference on silicon dielectric interfaces*. 2000. Raleigh, NC (USA): AVS.

57. Sorokin, P.P. and J.R. Lankard, *Stimulated Emission Observed from an Organic Dye Chloro-Aluminum Phthalocyanine.* Ibm Journal of Research and Development, 1966. **10**(2): p. 162-&.

58. Goodberlet, J., et al., *Femtosecond Passively Mode-Locked Ti-Al2o3 Laser with a Nonlinear External Cavity.* Optics Letters, 1989. **14**(20): p. 1125-1127.

59. Spence, D.E., P.N. Kean, and W. Sibbett, *60-fsec pulse generation from a self-mode-locked Ti:sapphire laser.* Opt. Lett., 1991. **16**(1): p. 42.

60. Coherent, *Ti:sapphire Mira 900 laser manual*.

61. Garfunkel, E.L., E. Gusev, and A. Vul, *Fundamental Aspects of Ultrathin Dielectrics on Si-Based Devices*. 1998, Dordrecht, the Netherlands: Kluwer Academic Publishers. 503.

62. McKee, R.A., F.J. Walker, and M.F. Chisholm, *Crystalline oxides on silicon: The first five monolayers.* Physical Review Letters, 1998. **81**(14): p. 3014-3017.

63. Cristoloveanu, S. and S.S. Li, *Electrical Characterization of SOI Materials and Devices*. 1995, Norwell, MA: Kluwer Academic Publishers.

64. Celler, G.K. and S. Cristoloveanu, *Frontiers of silicon-on-insulator.* Journal of Applied Physics, 2003. **93**(9): p. 4955-4978.

65. Gu, Y., T. Vu, and G.P. Li. *SOI Material Characterization Using Optical Second Harmonic Generation*. in *IEEE International SOI Conference* 1994.

66. Shabani, M.B., T. Yoshimi, and H. Abe, *Low-temperature out-diffusion of Cu from silicon wafers.* Journal of the Electrochemical Society, 1996. **143**(6): p. 2025-2029.

67. Beaman, K.L., et al., *Gettering of iron in silicon-on-insulator wafers.* Applied Physics Letters, 1997. **71**(8): p. 1107-1109.

68. Kononchuk, O., et al., *Diffusion of iron in the silicon dioxide layer of silicon-on-insulator structures.* Applied Physics Letters, 1998. **73**(9): p. 1206-1208.

69. M.H. Yang, A.W., M. Neuburger, R.S. Hockett. *SIMS measurements of metal contamination in SOI wafers*. in *Silicon-on-Insulator Technology and Devices XII: International Symposium*. 2005: Electrochemical Society.

70. Fleetwood, D.M., *Hydrogen-related reliability issues for advanced microelectronics.* Microelectronics Reliability, 2002. **42**(9-11): p. 1397-1403.

71. R. Pasternak, B.J., R. D. Schrimpf, D. M. Fleetwood, M. Alles, R. Dolan, R. Standley, N. Tolk. *Investigation of second-harmonic generation for SOI wafer metrology*. in *Silicon-on-Insulator Technology and Devices XII*. 2005.

72. M. L. Alles, R.P., N. H. Tolk, R. D. Schrimpf, D. M. Fleetwood, R. W. Standley. *Experimental Evaluation of Second Harmonic Generation for Non-Invasive Contamination Detection in SOI Wafers*. in *The 17th Annual IEEE/SEMI Advanced Semiconductor Manufacturing Conference*. 2006.

73. Y. Gu, T.V., G.P. Li. *SOI Material Characterization Using Optical Second Harmonic Generation*. in *IEEE International SOI Conference*. 1994.

74. M.L. Alles, R.P., X. Lu, N.H. Tolk, R.D. Schrimpf, D.M. Fleetwood, R.P. Dolan, R.W. Standley, *Second Harmonic Generation for Noninvasive Metrology of Silicon-on-Insulator Wafters.* IEEE TRANSACTIONS ON SEMICONDUCTOR MANUFACTURING, 2007. **20**(2): p. 107-113.

75. Z. Marka, S.K.S., W. Wang, S. C. Lee, J. Kavich, B. Glebov, S. N. Rashkeev, A. P. Karmarkar, R. G. Albridge, S. T. Pantelides, R. D. Schrimpf, D. M. Fleetwood, and N. H. Tolk, *Characterization of X-Ray Radiation Damage in Si/SiO2 Structures Using Second-Harmonic Generation.* IEEE TRANSACTIONS ON NUCLEAR SCIENCE, 2000. **47**(6): p. 2256-2261.

76. White, Y.V., et al., *Studies of charge carrier trapping and recombination processes in Si/SiO2/MgO structures using second-harmonic generation.* Applied Physics Letters, 2006. **88**(6).

77. C.L. Claeys, R.E.d.K., G.J. Declerck, ed. *The Si-SiO2 System*. 2nd ed., ed. P. Balk. 1988, Elsevier: Amsterdam.

78. G. F. Derbenwick, B.L.G., *PROCESS OPTIMIZATION OF RADIATION-HARDENED CMOS INTEGRATED CIRCUITS.* IEEE Transactions on Nuclear Science, 1975. **22**(6): p. 2151-2156.

79. Bl 鯏 hl, P.E. and J.H. Stathis, *Hydrogen Electrochemistry and Stress-Induced Leakage Current in Silica.* Physical Review Letters, 1999. **83**(2): p. 372.

80. Fleetwood, D.M. and N.S. Saks, *Oxide, interface, and border traps in thermal, N[sub 2]O, and N[sub 2]O-nitrided oxides.* Journal of Applied Physics, 1996. **79**(3): p. 1583-1594.

81. Miller, S.L., D.M. Fleetwood, and P.J. McWhorter, *Determining the energy distribution of traps in insulating thin films using the thermally stimulated current technique.* Physical Review Letters, 1992. **69**(5): p. 820.

82. Jellison, G.E. and F.A. Modine, *Optical functions of silicon between 1.7 and 4.7 eV at elevated temperatures.* Physical Review B, 1983. **27**(12): p. 7466.

83. Pasternak, R., X. Lu, and N.H. Tolk, *Temperature dependent second- and third-order optical nonlinear suscrptibilites in Si/SiO2.* Physical Review B, Submitted for publication.

84. Palik, E.D., *Handbook of the optical constants of solids*. 1985, San Diego: Academic Press.

85. Fox, M., *Optical Properties of Solids*. 2001: Oxford University Press Inc. 318.

86. Suzuki, T., et al., *Thermally enhanced second-harmonic generation from Si(111)-7 x 7 and "1 x 1".* Physical Review B, 1999. **59**(19): p. 12305-12308.

87. Lautenschlager, P., P.B. Allen, and M. Cardona, *Temperature-Dependence of Band-Gaps in Si and Ge.* Physical Review B, 1985. **31**(4): p. 2163-2171.

88. Allen, P.B. and V. Heine, *Theory of Temperature-Dependence of Electronic Band Structures.* Journal of Physics C-Solid State Physics, 1976. **9**(12): p. 2305-2312.

89. Levine, R.D. and R.B. Bernstein, *Molecular Reaction Dynamics and Chemical Reactivity*. 1987, Oxford: Oxford University Press.

90. Wang, J.F.T., et al., *Simplified bond-hyperpolarizability model of second harmonic generation: Application to Si-dielectric interfaces.* Journal of Vacuum Science & Technology B, 2002. **20**(4): p. 1699-1705.

91. Fischetti, M.V. and D.J. Dimaria, *Hot-Electrons in Sio2 - Ballistic to Steady-State Transport.* Solid-State Electronics, 1988. **31**(3-4): p. 629-636.

92. Tan, C.Z. and J. Arndt, *Temperature dependence of refractive index of glassy SiO2 in the infrared wavelength range.* Journal of Physics and Chemistry of Solids, 2000. **61**(8): p. 1315-1320.